Integrated Master in Chemical Engineering

# *Synthesis and characterization of a carbon supported transition metal phosphide for the oxygen evolution reaction*

## Master Thesis

by

**Maria Carolina Azevedo Lima Teixeira**

**Developed within the course of Dissertation**

held in

**DLR: Deutsches Zentrum für Luft- und Raumfahrt**




Supervisor at FEUP: Prof. Adélio Mendes

Supervisor at DLR: Dr. Norbert Wagner, M.Sc. Jan Majchel




Chemical Engineering Department

July 2019

## Acknowledgments

I would like to express my thanks to Professor K. Andreas Friedrich for allowing me to join the DLR team and grant me the opportunity to experience one of the most challenging experiences of my student life.

To my Professor Adélio Mendes I thank him for the fundamental tips, for constantly teaching me, supervising my work and always motivate me.

I am very thankful to my supervisor Dr. Norbert Wagner, for always being helpful, making me feel included in the team and making me feel comfortable with the work environment. I extent my heartly gratitude for sharing his invaluable knowledge and know-how with me.

I owe my deepest gratitude to Jan Majchel. I cannot quantify how much of a help he was during these past months. I thank him for the endless advice, unconditional and constant help and for the valuable scientific input into my work. I feel fortunate for having him as my supervisor.

I lend my regards to all the scientific staff at DLR, without whom the success of my thesis would not be complete.

My special thanks to Sofia Delgado for the fundamental guidance and her constant availability before and during this thesis.

To my college friends, Maria, Marta, Carla, Babi, for always encouraging me, push me further and sticking with me through every moment since the beginning. To my friend, Ambu, for constantly helping, supporting and motivate me throughout these months.

To my family, specially to my parents and brother, I cannot express how blessed i feel for everything they have done for me. They are my safe home, my best advisors, my biggest supports. Thank you for always pushing and believe in me. Without you, nothing would be possible. I am forever grateful to have you.

Professor Adélio Mendes, supervisor of this dissertation is an integrated member of LEPABE – Laboratory for Process Engineering, Environment, Biotechnology and Energy, financially supported by project UID/EQU/00511/2019 - Laboratory for Process Engineering, Environment, Biotechnology and Energy – LEPABE funded by national funds through FCT/MCTES (PIDDAC).

FCT Fundação para a Ciência e a Tecnologia

REPÚBLICA PORTUGUESA

# Abstract

Metal-air batteries have been received increasingly more attention because of their remarkably high energy density when compared to other types rechargeable batteries, such as lithium-ion. Even though, they are promising source of power for next-generation electronics, transportation and energy storage, they still have numerous technical challenges that must be overcome.

This work aims at to develop non-noble transition metal catalysts to improve the overall performance of metal-air batteries and provide an alternative to noble metal-based catalysts, which suffer from multiple disadvantages such as high cost and poor stability. Four catalysts were studied for the positive electrode targeting the enhancement of the oxygen reduction/evolution reactions. Transition-metal phosphides and carbon supported catalysts were synthesized, tested and characterized (*in situ* and *ex situ*). Based on literature information and on the experience of the research team, $Ni_2P$, $Ni_2P$/CNT, $Ni_2P$-Fe/CNT and $Ni_2P$-$Fe_2O_3$/CNT were prepared and characterized and their performance assessed.

It was proved that the addition of a carbon support improves the reactions current density and the synthesis of a bi-metal catalyst improves considerably the activity of catalysts. Furthermore, it was developed a new catalyst which improves considerably the performance of the oxygen evolution reaction compared with the reference Iridium black catalyst.


**Keywords:** Metal-air batteries, Oxygen evolution reaction, Oxygen reduction reaction, Catalysts synthesis, Electrocatalyst, Non-noble metal catalyst, Fe-based catalysts, Transition metal phosphides, RDE, Air cathode

## Resumo

Baterias de metal-ar cada vez mais têm recebido atenção graças à sua densidade energetica, notavelmente alta quando comparada a outros tipos de baterias recarregáveis, como as baterias de ião de lítio. São uma fonte promissora de energia para as próximas gerações de dispositivos eletrónicos, transporte e armazenamento de energia. No entanto, existem ainda vários problemas que necessitam de ser superados.

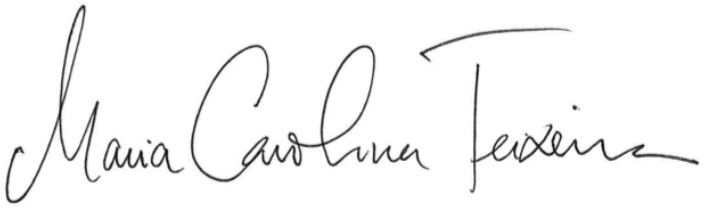
Este trabalho visa desenvolver catalisadores de metais de transição não nobres para melhorar o desempenho geral das baterias de metal-ar e fornecer uma alternativa aos catalisadores de metais nobres, que sofrem de múltiplas desvantagens, tal como o alto custo e a baixa estabilidade. Quatro catalisadores foram estudados para o elétrodo positivo, visando o aumento das reações de redução / evolução de oxigénio. Fosfetos de metal de transição e catalisadores suportados em carbono foram sintetizados, testados e caracterizados ( textit in situ e  textit ex situ). Com base nas informações da literatura e na experiência da equipa de pesquisa, $Ni_2P$, $Ni_2P$/CNT, $Ni_2P$-Fe/CNT and $Ni_2P$-$Fe_2O_3$/CNT foram preparados, caracterizados e testado o seu desempenho.

Foi provado que a adição de um suporte de carbono melhora a densidade de corrente das reações e a síntese de um catalisador bimetálico melhora, consideravelmente, a atividade dos catalisadores. Além disso, foi desenvolvido um novo catalisador que melhora substancialmente o desempenho da reação de evolução de oxigénio em comparação com o catalisador de referência, Iridium black.

**Keywords:** Baterias de metal-ar, Reação de evolução do oxigénio, Reação de redução do oxigénio, Síntese de catalisadores, Eletrocatalisador, metais de transição, Catalisadores à base de ferro, Fosfatos de metais de transição, elétrodo de disco rotativo, Cátodo de ar

# Declaration

I hereby declare, on my word of honour, that this work is original and that all non-original contributions were properly referenced with source identification.



30.06.19

Signature and date

# Contents

**1 Introduction** **1**

1.1 Framing and Presentation of the Work . . . . . 1

1.2 DLR - German Aerospace Center . . . . . 2

1.3 Work Contributions . . . . . 3

1.4 Thesis Organization . . . . . 3

**2 Context and State of the art** **4**

2.1 Metal-air batteries . . . . . 4

2.1.1 Metal electrode . . . . . 4

2.1.2 Air electrode . . . . . 4

2.1.3 Electrolyte . . . . . 7

2.2 Catalysts . . . . . 8

2.3 Thermodynamic Potential and kinetics . . . . . 9

2.3.1 Overpotential . . . . . 10

2.3.2 Kinetics . . . . . 11

2.4 Performance Evaluation . . . . . 12

2.4.1 Evaluation of ORR performance . . . . . 12

2.4.2 Evaluation of OER performance and iR drop . . . . . 13

**3 Materials and Methods** **15**

3.1 Rotating disk electrode . . . . . 15

3.2 Electrochemical characterization . . . . . 15

3.2.1 Cyclic Voltammetry . . . . . 15

3.2.2 Linear Sweep Voltammetry . . . . . 16

3.2.3 Double layer capacitance . . . . . 16

3.3 Physical characterization techniques . . . . . 16

3.3.1 SEM and EDX . . . . . 16

3.3.2 XRD . . . . . 17

3.3.3 XPS . . . . . 17

3.3.4 BET . . . 17
3.3.5 TGA . . . 18
3.4 Catalyst synthesis . . . 18
3.4.1 Unsupported catalyst synthesis, $Ni_2P$ . . . 18
3.4.2 Supported catalyst synthesis . . . 19
3.4.3 $Ni_2P$/CNT synthesis . . . 20
3.4.4 $Ni_2P$-Fe/CNT synthesis . . . 21
3.4.5 $Ni_2P$-$Fe_2O_3$/CNT via stirring and ultrassonication . . . 21
3.5 Catalyst ink and layer preparation . . . 22

**4 Results** **24**
4.1 Electrochemical characterization . . . 24
4.1.1 ORR activity . . . 24
4.1.2 OER activity and Tafel plot . . . 28
4.1.3 Capacitance measurements . . . 31
4.2 Ultra-sonication vs. stirring for $Ni_2P$-$Fe_2O_3$/CNT . . . 32
4.3 Physical characterization . . . 34
4.3.1 SEM Results . . . 34
4.3.2 EDX Results . . . 36
4.3.3 XRD Results . . . 40
4.3.4 XPS Results . . . 42
4.3.5 TGA Results . . . 43
4.3.6 BET Results . . . 44

**5 Conclusion** **46**

**6 Assessment of the work done** **47**
6.1 Objectives Achieved . . . 47
6.2 Limitations and Future work . . . 47
6.3 Final Assessment . . . 47

**7 References** **48**

**A Appendix** **53**

A.1 Other Results . . . . . 53

A.2 Equipment used . . . . . 56

# Notation and Glossary

*Latin Letters*

| | | |
|---|---|---|
| $B$ | Tafel slope | $\mathrm{mV\ dec^{-1}}$ |
| $C_{O_2}$ | Concentration of $O_2$ molecules | $\mathrm{cm^2\,s^{-1}}$ |
| $c_{dl}$ | Double-layer Capacitance | $\mu\mathrm{Fcm^{-2}}$ |
| $D_{O_2}$ | Diffusion coefficient of $O_2$ | $\mathrm{cm^2\,s^{-1}}$ |
| $E$ | Electrode potential | V |
| $E^0$ | standard potential of the redox reaction | V |
| $E_{onset}$ | onset potential | V |
| $E_{1/2}$ | half-wave potential | V |
| $F$ | Faraday constant | $96\,485\,\mathrm{C\ mol^{-1}}$ |
| $i$ | Current | A |
| $j$ | Current density | $\mathrm{A\,cm^{-2}}$ |
| $j_0$ | Exchanged current density | $\mathrm{mAcm^{-2}}$ |
| $j_L$ | diffusion-limiting current density | $\mathrm{mAcm^{-2}}$ |
| $n$ | Number of moles of electrons transferred | mol |
| $P$ | Pressure | bar |
| $R$ | Universal Gas Constant | $\mathrm{J\,mol^{-1}\,K}$ |
| R | Ohmic resistance | $\Omega$ |
| $T$ | Temperature | K |

*Greek Letters*

| | | |
|---|---|---|
| $\eta$ | Overpotential | V |
| $\nu$ | Kinematic viscosity | $\mathrm{cm^2\,s^{-1}}$ |
| $\omega$ | angular rotation | $\mathrm{rads^{-1}}$ |

***List of Acronyms***

| | |
|---|---|
| BET | Brunauer–Emmett–Teller |
| BV | Butler-Volmer |
| CE | Counter Electrode |
| CNT | Carbon Nanotubes |
| CV | Cyclic Voltammetry |
| ECSA | Electrochemically Active Surface Area |
| EDX | Energy-dispersive X-ray |
| EIS | Electrochemical Impedance Spectroscopy |
| ESB | Energy Selective Backscattered |
| GCE | Glassy Carbon Electrode |
| GDE | Gas Diffusion Electrode |
| GDL | Gas Diffusion Layer |
| KOH | Potassium Hydroxide |
| K-L | Koutecky-Levich |
| LABs | Lithium-ion batteries |

| | |
|---|---|
| LSV | Linear Sweep Voltametry |
| OER | Oxygen Evolution Reaction |
| ORR | Oxygen Reduction Reaction |
| PTFE | Polytetrafluoroethylene |
| RDE | Rotating Disk Electrode |
| RHE | Reversible Hydrogen Electrode |
| SE | Secondary Electron |
| SEM | Scanning Electron Microscopy |
| SSA | Specifc Surface Area |
| TGA | Thermogravimetric Analysis |
| TMP | Transition Metal phosphides |
| TPB | Triple-Phase-Boundary |
| XPS | X-ray Photoelectron Spectroscopy |
| XRD | X-ray Powder Diffraction |
| WE | Working Electrode |

# 1 Introduction

## 1.1 Framing and Presentation of the Work

Throughout the years, the worldwide demand for energy as been constantly increasing and with it comes the urge of development of new technologies in alternative to non-renewable sources as fossil fuels. The awareness for environmental issues is, as well, one of the biggest concerns of society and there is a big need for environmental friendly power sources.[1]

Electrochemical conversion technologies, such as batteries with high power density and with a rapid discharge capability, are among the key energy storage for the burst of energy for devices for the next generation of electronics and electric vehicles (EVs).

Since the now available lithium-ion batteries (LABs) are not sufficient enough to meet the demands of markets such as the EVs which have limited driving due to the low specific energy density of the LABs, new systems are in process of development.

Metal-air batteries such as lithium-air, zinc-air, have attracted much attention due to their high energy density when compared to other types of rechargeable batteries, figure 1, making them a promising candidate to substitute the now available LABs. [1][2] Metal-air batteries use oxygen from the air, low weight metal as the negative electrode and porous, light-weight, carbon based materials as the positive cathode making them lighter batteries. [3]

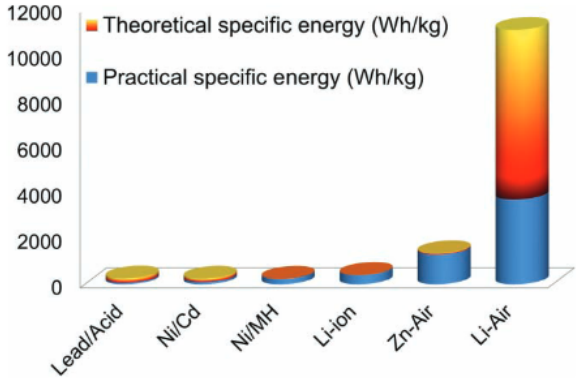



Figure 1: Theoretical and practical energy densities of different types of batteries.[4]

Although they are a great candidate, having a theoretical energy density almost as high as

gasoline, they still face a lot of challenges being the biggest issue associated with the sluggish kinetics of the air cathode. Electrocatalysts for the oxygen evolution reaction (OER) and oxygen reduction reaction (ORR), during charge and discharge in batteries, are limited by the high existing overpotentials on the positive electrode . [5]

Noble metal based catalysts, such as Pt, Pt-based alloys (PtAu) are considered the best catalysts for ORR, while $RuO_2$ and $IrO_2$ are considered the premium catalysts for OER. However, these noble metal-based catalysts suffer from multiple disadvantages, including high cost, low selectivity, poor stability, detrimental environmental effects and limited reserves have precluded these renewable energy technologies from large-scale commercial applications.[6][7]

Nevertheless, a lot of effort has been made throughout the years to develop bifunctional nonprecious-metal electrocatalysts that can replace noble-metal catalysts and accelerate the ORR and OER process in order to significantly increase the rate capability, energy efficiency and operational life of metal-air batteries and improve mass production of clean and renewable energy.[7]

This thesis aims to develop non noble metal catalysts to improve the reactions kinetics in metal-air batteries and substitute expensive noble-metal catalysts.

## 1.2 DLR - German Aerospace Center

The German Aerospace Center, also known as DLR, was created in Göttingen in 1907 and it is the Federal Republic of Germany national research center for aerospace, energy and transportation.

DLR is present in 20 location around Germany along with international offices in Brussels, Paris, Tokyo and Washington D.C.

This master thesis was held in the Institute of Engineering Thermodynamics, in Stuttgart. The DLR site in Stuttgart was first established in 1954 at Stuttgart airport and, since 1961, it is located in Stuttgart-Vaihingen. It counts with more than 700 employees in six institutes. In the Engineering Thermodynamics Institute it is promoted the development of electrochemical and thermochemical energy storage and conversion devices such as electrolyzers, fuel cells and advanced batteries. It also investigates efficiency, cost and sustainability of future energy systems.[8]

## 1.3 Work Contributions

DLR purses the development of performance improvement for metal-air batteries. A lot of studies have been made throughout the years to synthesize catalysts which improve the sluggish kinetics of metal-air batteries. During the development of this project, I designed two new catalysts that could improve the metal-air batteries kinetic reaction, synthesized them and performed all of the electrochemical measurements stated. All of the *ex situ* measurements were performed by laboratory technicians, responsible for each measurement.

## 1.4 Thesis Organization

This thesis is divided into five different chapters.

The first chapter, Introduction, gives a brief overview and helps to understand the necessity of this work. The second one, State of the art, is a gathering of important concepts related to metal-air batteries and gives the reader a contextualization of the subject. In the Materials and Methods chapter, third one, it is explained the procedures done and methods used to synthesize and characterize the different catalysts studied. The following chapter, the fourth, is presented all the obtained results.

The conclusion of this work is presented in the fifth chapter and finally as the last chapter, Assessment of the work done, describes the objectives achieved and presents a personal opinion about this project.

# 2 Context and State of the art

## 2.1 Metal-air batteries

Metal-air batteries are electrochemical cells that use a metal as anode and have the particularity of using $O_2$ drawn from the surrounding environment at the cathode. They convert the chemical energy of electrochemical reactions, occurring at its electrodes, into electrical energy.[9] The distinguishable characteristic of this type of batteries is the abundant and free availability of the cathode material, the oxygen.[4]

The cell configuration of conventional rechargeable batteries are based on three main active components, the negative and positive electrode and the electrolyte, which will be further explained in the following sections.[10]

### 2.1.1 Metal electrode

There are several kinds of metal-air batteries based on the metal species of the anode. Most frequently, the metal used is lithium, zinc, aluminum and magnesium and the characteristic reactions mechanisms of the battery vary according to the metal used.[4] Nevertheless, during discharging the reaction of metal oxidation is common to all of metal anodes and can be generalized as equation (1). In rechargeable batteries the reaction is reversed and the metal will be then reduced while the cathode is being oxidized.

$$\mathrm{M} \leftrightarrow \mathrm{M}^{z+} + z\mathrm{e}^{-} \tag{1}$$

### 2.1.2 Air electrode

The air electrode, which is usually referred as the gas diffusion electrode (GDE), is divided into a three layer electrode system, consisting in a gas diffusion layer (GDL) responsible for oxygen adsorption (and its distribution to the catalyst sites), a catalyst active layer responsible for catalyzing the reactions, and a current collector for electron conduction.[11]

During the discharge process, the oxygen from the atmosphere diffuses into the porous electrode, due to pressure difference, and it is reduced at the air cathode by accepting the electrons released from the metal anode during its oxidation process. This reaction is known as ORR. In the charging process, while the metal-ion is being reduced, the oxygen is being evolved at the cathode, OER. [2][3]

Regarding the redox reactions, the ORR can proceed in two different paths. The four electron path, presented in equation (2). [12]

$$O_2 + 2H_2O + 4e^- \rightleftharpoons 4OH^-; E^0 = 0.401\,\mathrm{V}\ vs.\ \mathrm{SHE} \tag{2}$$

and the two-electron path, equation 3, where $O_2$ is reduced to peroxide ion.

$$O_2 + H_2O + 2e^- \rightarrow HO_2^- + OH^-; E^0 = 0.076\,\mathrm{V}\ vs.\ \mathrm{SHE} \tag{3}$$

The two-electron pathway is followed by further reduction, presented in the following equation.

$$HO_2^- + H_2O + 2e^- \rightarrow 3OH^-; E^0 = 0.878\,\mathrm{V}\ vs.\ \mathrm{SHE} \tag{4}$$

Even more, it can also happen a disproportionation reaction presented in equation 5.

$$2HO_2^- \rightarrow 2OH^- + O_2 \tag{5}$$

The OER overall reaction is the reverse reaction of ORR reaction (2), where $O_2$ is produced. [13] However, the OER mechanism is different depending on the catalyst. Many research groups have proposed possible mechanisms. Possible reaction intermediates are OH, O and OOH and the mechanism might follow the reaction steps presented below. [14][15][16]

$$4OH^- \rightarrow OH_{ads} + 3OH^- + e^- \tag{6}$$

$$OH_{ads} + 3OH^- + e^- \rightarrow O_{ads} + H_2O + 2OH^- + 2e^- \tag{7}$$

$$O_{ads} + H_2O + 2OH^- + 2e^- \rightarrow HOO_{ads} + H_2O + OH^- + 3e^- \tag{8}$$

$$HOO_{ads} + H_2O + OH^- + 3e^- \rightarrow O_2 + 2H_2O + 4e^- \quad (9)$$

This reactions can only take place at confined spatial sites, which is called the triple phase boundary (TPB). The TPB is where the catalytic electrode is simultaneously interfaced with liquid electrolyte and gaseous $O_2$. These spaces hold a complex interplay between the reaction processes that occur at the catalyst/electrolyte interface and the reactants diffusion processes through this same interface. [13] [17] A simplified scheme of the TPB is shown in figure 2.

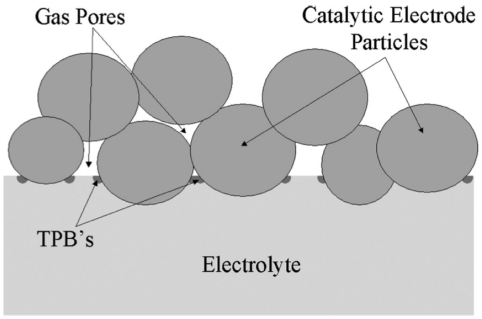



Figure 2: Schematic representation of the TPB system.[17]

The thin and highly porous GDL allows the flow of $O_2$ in order to accomplish high current densities during discharge process. [1][18] The GDL should also be hydrophobic to avoid flooding, ensuring the coexistence of gas and liquid phase in the porous structure. Agents, such as PTFE, can be impregnated and guarantee the hydrophobic characteristic. [1] The degree of hydrophobicity has to be taken in consideration since it influences the battery polarization behavior. At low current densities, the major contribution of PTFE content is to the degree of hydrophobicity and porosity affecting the gas permeability (mass transfer).[1] Increasing PTFE content in the electrode reduces porosity. However, hydrophobicity is increased. This is called the activation loss controlled region. [11] At higher current densities, the ohmic loss controlled region takes over electrical conductivity (Ohmic resistance), but also in terms of the gas permeability (mass transfer).[1] Moreover, the binder improves the mechanical stability of the electrode and maintains open pore structures due to the hydrophobic effect, when an aqueous electrolyte is used. [18] [5]

To prevent the particles from passing through, the air cathode is also constituted by a separator, a physical barrier that, besides preventing the contact between the two electrodes, allows the

ionic flow.[3]

### 2.1.3 Electrolyte

The electrolyte plays a vital role as a medium to transport metal ions and dissolved oxygen, affecting the battery electrochemistry. Metal–air batteries are, frequently, classified according to the nature of its electrolyte. The most common ones are aqueous, nonaqueous, or even solid-state and hybrid systems of the ones mentioned before.[13] [2]

The electrolyte affects the battery performance, therefore it should possess properties such as high oxygen solubility and diffusivity, low volatility and viscosity. [13] With that in mind, and knowing alkaline media provides a less corrosive environment to the catalysts, as well as better kinetics when compared with acidic media, [10] concentrated pothassium hydroxide (KOH) solutions are usually used due to the highest ionic conductivity and the lowest viscosity, providing better electrochemical kinetics and mass transport. [1]

On the other hand, alkaline electrolytes medium can have negative aspects such as the reaction of carbon dioxide from the air with the alkaline electrolyte producing potassium carbonate which precipitates inside the air electrode, which can, not only block the pores of the electrode, but also lead to irreversible failure of air cathode [3]

In figure 3, there is a schematic representation of a metal-air battery in aqueous electrolyte, where is illustrated the $O_2$ diffusion from the outer atmosphere and adsorption on the catalyst surface, reduction of the metal with transfer of electrons from the metal anode to the $O_2$ molecules through an external current, breaking of the oxygen bond, and the desorption of the hydroxyl ion product from the catalyst surface to the electrolyte.[2][13]

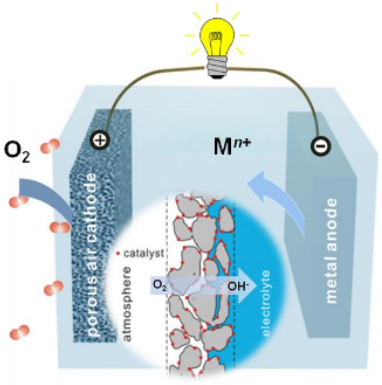



Figure 3: Configuration and operating principle for an aqueous metal-air battery.[19]

## 2.2 Catalysts

Both ORR and OER show high overpotential, as a result power density and current rates are affected. It has been demonstrated that both overpotentials can be dramatically decreased by the use of catalytic materials in the air electrode.[1] Hence, ORR and OER catalysts are always applied to lower the activation energy and increase the conversion rate of the electrochemical reactions. [1]

As before mentioned, noble metal catalysts have multiple disadvantages, therefore different approaches have been taken in consideration throughout the years in order to find low-cost, efficient and stable bifunctional catalysts which is particularly difficult, because good catalysts for ORR cannot drive OER and vice versa.[11]

Platinum based catalysts and noble metal catalysts such as Au and Pd have been known as the best catalyst for the ORR. However, due to the high-cost, scarcity, degradation and performance loss under OER conditions, there is the need to find other catalysts.

Several types of non-precious catalysts have been studied, including transition metals, like Ni and Fe, perovskites and transition metal spinel oxides such as manganese oxide ($MnO_2$) and cobalt oxide ($Co_3O_4$) have been widely considered as a promising candidates because they are relatively inexpensive and present a good ORR activity. Ag is also a promising candidate because it is less expensive and has similar reaction mechanisms and kinetics for ORR compared to Pt.[20][10][21] [5] Transition-metal electrocatalysts (such as metal phosphides ($Ni_2P$), sulfides,

and oxides (NiOx, $Fe_2O_3$, $Co_3O_4$, Ni-oxyhydroxides) which are very good for OER are poor for ORR.[22]

The combination of transition metals and carbon nanomaterials, including carbon nanotubes (CNT), graphene sheets and three-dimensional carbon architectures are also a promising strategy. They are explored owing to their excellent quality as a support material, high electrical conductivity and extremely corrosion resistance in basic environments, as well as being less expensive in comparison to noble metals. [1][11][21]

## 2.3 Thermodynamic Potential and kinetics

In a typical electrochemical cell there are two electrodes and, at each one, an electrochemical reaction occurs. This reaction is called a half cell reaction, also known as a redox (oxidation-reduction) reaction. This type of reaction involves transfer of electrons between two species changing the oxidation states. The reduction of an oxidized element (Ox), can be represented by equation (10).

$$\mathrm{Ox} + n\mathrm{e}^- \rightleftharpoons \mathrm{Red} \tag{10}$$

Where *Red* represent the reduced form of the species by accepting a certain number ($n$) of electrons. This reactions are usually reversible, meaning that the oxidized form of the solution species can be regenerated from the reduced form.

The potential at each electrode can be then expressed according to Nernst as equation (11).

$$E = E^0 + \frac{RT}{nF}\ln\frac{C_{\mathrm{Ox}}}{C_{\mathrm{Red}}} \tag{11}$$

The applied potential ($E$) is dependent on the standard potential of the redox reaction ($E^0$), on the absolute temperature ($T$), the universal gas constant ($R$), Faraday constant ($F$), on $n$ and on the concentrations of oxidized and reduced reagents, ($C_{\mathrm{Ox}}$) and ($C_{\mathrm{Red}}$) respectively.[14]

### 2.3.1 Overpotential

The energy conversion in an electrochemical process is often limited by high-activation barrier and, in order to overcome the kinetic barrier of the reaction and drive the reactions, it is necessary to apply a higher potential than that at equilibrium.[14]

The difference between the applied potential and the potential under equilibrium conditions is denominated as overpotential($\eta$) and it is illustrated as equation (12). [2]

$$\eta = E - E_{eq} \tag{12}$$

There are different kind of overpotential influences in the overall overpotential. The three major contributors for the impedance are classified as the ohmic overpotential ($\eta_\Omega$), activation overpotential (charge tranfer kinetics) ($\eta_{ac}$), and concentration overpotential (mass-transport limitation) $\eta_\mathrm{L}$ .[23] [24]

The $\eta_\Omega$ takes into account the electrolytic resistivity of the anode and cathode bipolar plates regarding electron migration. [12] The $\eta_\mathrm{ac}$ is the potential required to overcome the activation energy of the reaction to produce a specified current. [23] The $\eta_\mathrm{L}$ is caused by the concentration gradient of reactants, or products, in the bulk electrolyte to the electrode surface, further explained in the following section.[25]

The overall overpotential, equation (13), of the electrochemical cell is the summation of the three overpotential contributions. [23]

$$\eta = \eta_\Omega + \eta_{ac} + \eta_\mathrm{L} \tag{13}$$

As electrochemical processes involve transfer of charged species in the interface region between the electrode and the electrolyte, where reactions take place, there is accumulation and nonuniform distribution of charged species.[23] Positive charges accumulate on one side of the interface, due to chemical interaction, while negative charges collect on the other side (moving fluid). The charge difference between the interfaces is known as the electrical double layer (EDL), figure 4. The thickness of the diffusion layer corresponds to the region where the concentrations of the charged species is different from the concentration of the bulk ones and it is also commonly

referred as the Nernst diffusion layer. [23] [26]

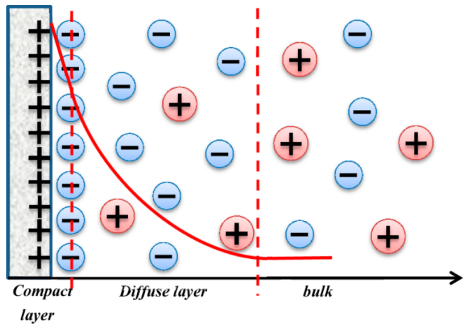



Figure 4: Electrical double layer.[27]

### 2.3.2 Kinetics

When mass transport is not a rate-determining step, the relationship between the current, i, and the activation overpotential, $\eta_{ac}$, follows the Butler-Volmer (BV) equation for low $\eta$. Equation (14) describes the electrical current (j) on an electrode. [23][24]

$$j = j_0 \left[ \exp(\frac{\alpha_a n F \eta}{RT}) - \exp(-\frac{\alpha_c n F \eta}{RT}) \right] \tag{14}$$

The j is the difference between the anodic and cathodic current densities, being the first term the metal dissolution, while the second term represents the metal deposition. $j_0$ represents the exchange current density, $\alpha_a$ and $\alpha_c$ are the anodic and cathodic charge transfer coefficient, respectively. [14][12]

At high $\eta$, where the reaction in the electrode becomes irreversible, it can be derived from the anodic and cathodic current densities in the BV equation, the Tafel equation (15), which relates the current and the applied electrochemical potential.[14]

$$\eta = \frac{RT}{nF\alpha_c} \ln j_0 - \frac{RT}{nF\alpha_a} \ln j = a - b \ln j \tag{15}$$

A plot of the BV equation is represented in figure 5. For low $\eta$, $i_c$ represents the cathodic current, while $i_a$ represents the anodic current for high $\eta$. For $\eta$=0 the current is defined as exchanged current density, $j_0$.

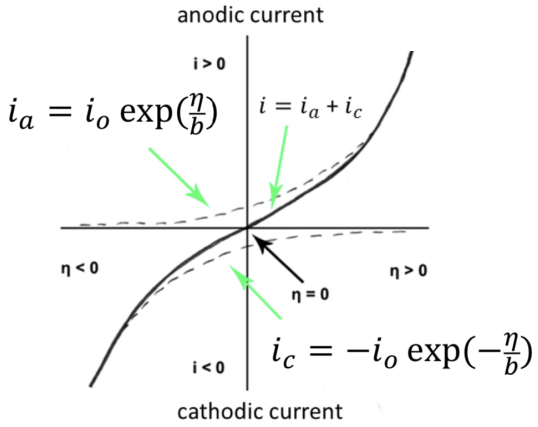



Figure 5: BV plot for low and high η. [28]

## 2.4 Performance Evaluation

The performance characteristics of metal-air batteries can be determined by typically done measurements such as Linear Sweep Voltametry (LSV) and Cyclic Voltametry (CV), which are performance indicators of the kinetics of the ORR and OER reactions, respectively, allowing the comparison between different catalysts. [23]

### 2.4.1 Evaluation of ORR performance

As it was previously mentioned, the ORR reaction mechanism can follow two different paths. Catalysts which induce the 4 electron reduction path of oxygen are highly preferred not only because of the higher energy conversion but also no significant adverse effect on the stability of catalyst as it can happen in 2 electron reduction path owing to the high yield of $HO_2^-$.[12]

The electron transfer number per oxygen molecule ($n$) involved in ORR, directly correlated with the selectivity of the catalyst, can be determined by Koutecky-Levich (K-L) equation, equation (16). [10]

$$\frac{1}{j} = \frac{1}{j_K} + \frac{1}{j_M} \Leftrightarrow \frac{1}{j} = \frac{1}{j_K} + \frac{1}{B_L w^{1/2}} \tag{16}$$

Where $j$ stands for the measured current, $j_K$ is the kinetic current density, ω is the angular rotation rate of the electrode in $\mathrm{rad\,s^{-1}}$ and $j_M$ is the mass transport current which can be calculated from the so-called K-L plot where the inverse measured current is plotted versus the

inverse square root of the rotation rate, $w^{1/2}$, being the slope the inverse of the Levich Constant, $B_L$. The respective $n$ relative to reactions in chapter 2.1.2, can be then calculated from equation (17).[29] [30] [10]

$$B = 0.62nFC_{O_2}D_{O_2}^{2/3}\nu^{-1/6} \tag{17}$$

In equation (17), $F$ refers to the the Faraday constant, $D_{O_2}$ is the diffusion coefficient of oxygen ($1.8\text{x}10^{-5}$ $\text{cm}^2\,\text{s}^{-1}$), ν is the kinematics viscosity of the solution ($1.0\text{x}10^{-2}$ $\text{cm}^2\,\text{s}^{-1}$) and $C_{O_2}$ is the bulk concentration of $O_2$ molecules ($7.8\text{x}10^{-7}$ $\text{mol}\,\text{cm}^{-3}$). The values of these coefficients are referred to 1 M KOH solution, since it was the concentration studied for easier comparison with other state of the art catalysts. [29]

In figure 6, there is a representation of a common ORR curve. The performance indicators that can be read in this type of curves are the potential at which the reaction starts, called the onset potential $E_{\text{onset}}$ , the half-wave potential $E_{1/2}$, which is the potential at which the current is equal to one half of the diffusion-limiting current density $j_L$, and the η. [10]

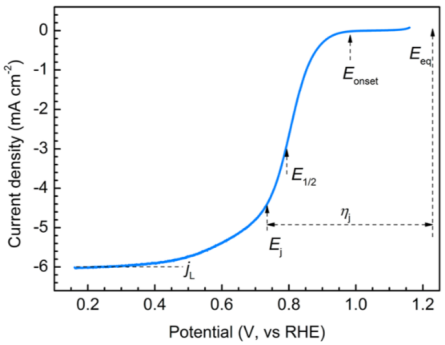



Figure 6: Typical LSV polarization curve. [10]

### 2.4.2 Evaluation of OER performance and iR drop

The major indicators for OER activity involve the $E_{\text{onset}}$, kinetic η and exchanged current density, $j_0$.[31]

However, whenever a current is passing through the circuit there is an extra resistance induced by the electrolyte resistance. This uncompensated resistance, often named as ohmic resistance

(R), leads to an additional voltage drop called iR drop. [32] This will cause an error in the experiments. Therefore, in order to determine the true potential it is subtracted to the applied potential $E_a$, the current measured ($i$) times the R measured. Equation (18) shows the correction necessary to make. [33]

$$E_p = E_a - i\mathrm{R} \tag{18}$$

The Tafel slope, $B$ is also an important parameter to test OER activity. It is obtained from the Tafel plot, which is a representation of $\eta$ vs. log$i$, directly specifies how much overpotential it is needed to increase the reaction rate by a factor of ten. It provides insightful information towards the mechanism of the reaction. [27] [34] Tafel slopes are closely related to the electrons involved in the reaction, therefore different Tafel slopes implicate different rate-determining steps and a smaller Tafel slope predicts a possible good catalyst. In figure 7, it is represented the Tafel plot with two different Tafel slopes.[14]

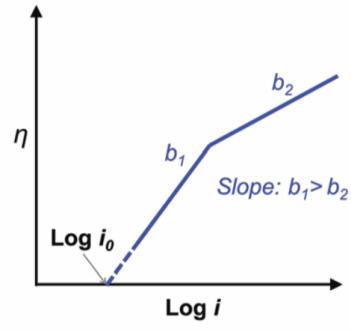



Figure 7: Representation of Tafel plot with two different slopes.[14]

# 3 Materials and Methods

## 3.1 Rotating disk electrode

To characterize the efficiency of an electrocatalytic material it was used a rotating disk electrode (RDE), a three-electrode configuration system. It measures the electrical current flow between the working electrode (WE) and the counter electrode (CE). The potential is measured between the WE and a reversible hydrogen electrode (RHE). The WE, CE and RHE are submersed in 1 M KOH electrolyte, as alkaline environments own improved kinetics in comparison to acidic media. In the RDE used for the experiments presented in this thesis it was used a Pt foil as CE. [1][20] In the Annex it is possible to find a picture of the RDE in which the experiments for this thesis were conducted, figure 43.

Different electrochemical tests were performed in RDE. It was chosen a potential region in which a redox reaction, ORR or OER, take place using a specific scan rate. The current was measured by a Zahner IM6 potentiostat. The response obtained in the cycling region allows to understand the mechanism and reactions that might occur.

## 3.2 Electrochemical characterization

### 3.2.1 Cyclic Voltammetry

To evaluate the electrochemical activity of the catalyst for the OER, it was firstly purged $N_2$ into the electrolyte for 15 min to guarantee a saturated environment. The working temperature was 25°C. Afterwards, it was performed 3 cycles with potentials ranging from 1.2 V to 1.65 V, such that the reaction could happen. The cycles were performed with a scan rate of $5\,\mathrm{mV\,s^{-1}}$ and it was applied a rotation speed of 1600 rpm in order to eliminate mass-transfer limitations. For OER evaluation it was plotted the $1^{st}$ cycle.

### 3.2.2 Linear Sweep Voltammetry

The working electrode was scanned at $5\,\mathrm{mV\,s^{-1}}$, for 2 cycles in a potential range between 0.2 V and 1.1 V in order to evaluate the ORR performance. The test was performed for different rotations speeds, 400, 900, 1600 and 2500 rpm. The experiments were performed at 25°C in $O_2$ saturated atmosphere (15 min saturation). The output was then used for the evaluation of the number of electron transferred per catalyst during the reaction. Regarding the ORR evaluation it was consider for plotting the $2^{nd}$ cycle.

### 3.2.3 Double layer capacitance

The capacitive double layer ($c_{dl}$) measurements are commonly performed since the $c_{dl}$ value is expected to be linearly proportional to the electrochemically active surface area (ECSA). The CV technique, at 0 rpm and potential window between 0.95 V and 1.05 V with various scan rates raging from $10\,\mathrm{mV\,s^{-1}}$ to $1600\,\mathrm{mV\,s^{-1}}$, were done. These measurements are performed in a potential window where there is no current related to charge transfer process flowing, in order to avoid kinetic processes. It is also commonly accepted that the ECSA has a linear relationship with the EDL capacitance caused by the inter-facial charging process. [31]

## 3.3 Physical characterization techniques

To have a better understanding of the catalysts performance and comprehend the different behaviours of the catalysts, indirect *ex situ* characterization techniques were done.

### 3.3.1 SEM and EDX

Scanning electron microscopy (SEM) is an *ex situ* technique that allows to understand the morphology of the catalysts regarding the homogeneity, elements distribution, pore distribution, agglomerates formed and elements size.

The distance between the lenses and the catalyst powder was kept between 4.0-8.0 mm distance and the electron beam with a voltage beetween 1.00 and 3.00 kV. The images were recorded

based on the energy selective backscattered (ESB) and Secondary electron (SE) to increase the contrast between the different elements.

An Energy Dispersive X-Ray Spectroscopy (EDX) was also used, combined with SEM measurements, to provide elemental identification as well as quantitative composition information.The catalysts were spread on a carbon tape and it was sorted different areas with different sizes and compositions. The lens was kept between 7.8 and 8.1 mm distance and the X-ray beam 15 kV.

### 3.3.2 XRD

X-ray powder diffraction (XRD) was used for phase identification of the materials. The measurements for $Ni_2P$ and $Ni_2P$/CNT were perfromed using a Cu-K$\alpha$ source of electrons, while for $Ni_2P$-Fe/CNT, $Ni_2P$-$Fe_2O_3$/CNT, Fe/CNT and $Fe_2O_3$/CNT the source of the electron beam was Co.

### 3.3.3 XPS

The x-ray source used for X-ray photoelectron spectroscopy (XPS) measurements was Al K-alpha and the pass energy used was 60 eV. It was assigned the binding energies of Ni2p (from 890 eV to 840 eV), for Fe2p (730 eV to 690 eV) and for P2p (from 140 eV to 125 eV).

### 3.3.4 BET

Brunauer–Emmett–Teller (BET) measurements were done to obtain the specific surface area (SSA) of the catalysts, giving insight on its porosity. All the samples were prepared by being dried in vacuum at 40°C. The measurements regarding $Ni_2P$/CNT and $Ni_2P$-$Fe_2O_3$/CNT were performed in $N_2$ atmosphere, while $Ni_2P$ and $Ni_2P$-Fe/CNT measurements were carried out in Kr atmosphere.

### 3.3.5 TGA

Thermal gravimetric analysis (TGA) is a method of thermal analysis and it was used to determine the mass percentage of CNT on the material. It was used a heat range of 5 K/ min in an Argon atmosphere.

## 3.4 Catalyst synthesis

In this thesis it was synthesised the 4 different idealized catalysts, being them $Ni_2P$, $Ni_2P$/CNT, $Ni_2P$-Fe/CNT and $Ni_2P$-$Fe_2O_3$/CNT, as well as 2 Fe based catalysts supported on CNT, Fe/CNT and $Fe_2O_3$/CNT.

### 3.4.1 Unsupported catalyst synthesis, $Ni_2P$

For the synthesis of $Ni_2P$, it was weighted and griended 0.3 g of $NiCl_2{\cdot}6H_2O$[1] and 0.66 g of $NaH_2PO_2{\cdot}H_2O$[2]. Afterwards, it was submitted to a heat treatment at 250 °C during 1 h in $N_2$ atmosphere, in a tubular furnace. The resultant powder was grinded and cleaned with water to remove especially salts, 3 times in a centrifuge rotating at 7600 rpm during 4 min. Was then rinsed with Ethanol and dried at 60 °C in an oven at ambient pressure.

In figure 8 there is the synthesis flowchart. This synthesis process was based in literature [35].

[1] Alfa Aesar®; Nickel(II) chloride hexahydrate, 99.95% (metals basis); 7791-20-0
[2] Acros Organics; Sodium hypophosphite monohydrate; 10039-56-2

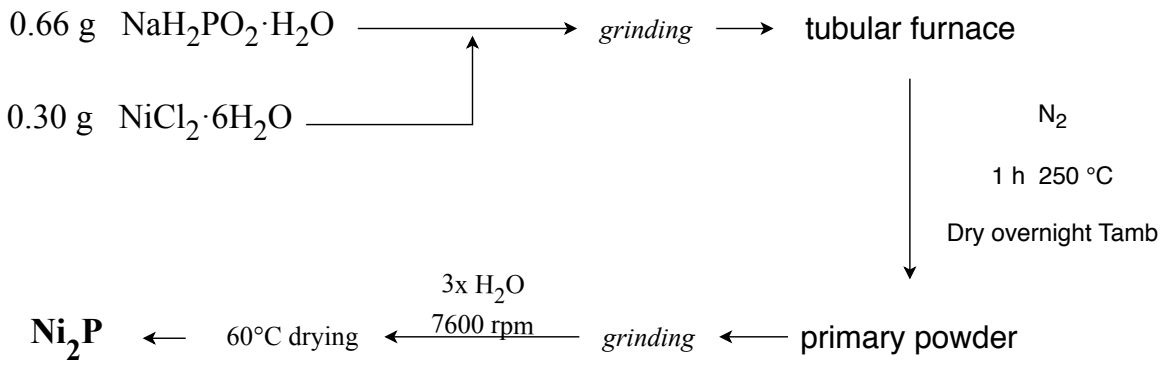



Figure 8: $Ni_2P$ synthesis procedure flowchart.

### 3.4.2 Supported catalyst synthesis

For all the different supported catalysts synthesized in the study it was used as a support CNT[3].

For the synthesis of Fe/CNT and $Fe_2O_3$/CNT, it was used 450 mg of multi-walled CNT (with an O.D. of 7-15 nm, I.D. of 3-6 nm and length of 0.5-200 $\mu$m), 1.44 g of $Fe(NO_3)_3{\cdot}9H_2O$ [4]. Both materials were dissolved, separately, in 50 and 150 ml of ethanol, respectively and sonicated for 45 min each. They were then mixed and sonicated for 1 h. The aim of ultrasonication is to have homogeneous distribution of particles and hence decreasing the possibility of agglomeration. The mixture was then kept in an oven at 60 °C at atmospheric pressure to evaporate the ethanol.

For the synthesis of $Fe_2O_3$/CNT, the residue obtained from the previous steps was calcinated for 3.5 h at 350 °C in an oven in normal atmosphere air.

While for the synthesis of Fe/CNT it was submitted to a heat treatment in a tubular furnace for 3.5 h at 350 °C under 95% $N_2$ and 5% $H_2$ atmosphere.

The process of synthesis and quantities used were adapted from literature. [36] The flowchart for the synthesis procedure for both catalysts is explained in figure 9.

[3]Sigma-Aldrich; Carbon nanotube, multi-walled; 308068-56-6
[4]ACROS Organics; Iron(III) nitrate nonahydrate, 99+%; 7782-61-8

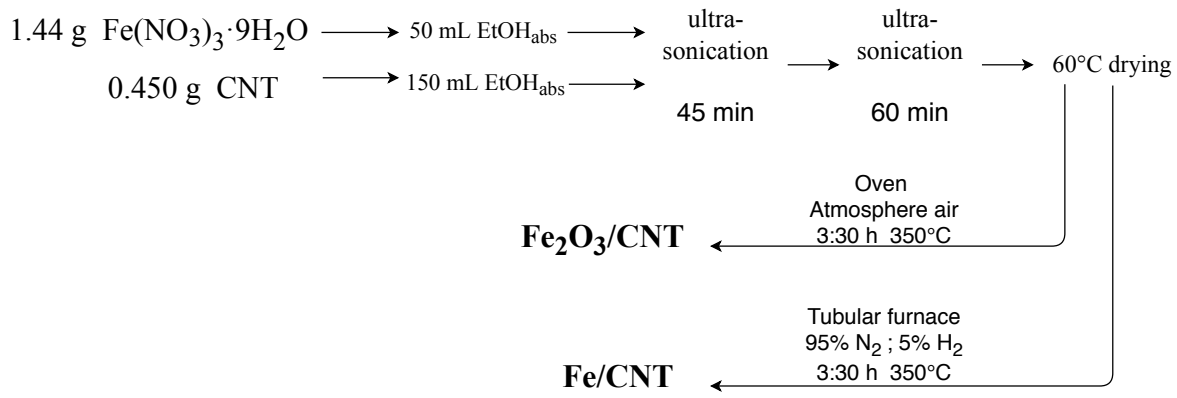



Figure 9: $Fe_2O_3$/CNT and Fe/CNT synthesis procedure flowchart.

### 3.4.3 $Ni_2P$/CNT synthesis

For the syntesis of $Ni_2P$/CNT it was weighted 0.600 g of $NiCl_2{\cdot}6H_2O$ and stirred in solution with 30 ml of $EtOH_{abs}$[5] it was then added 0.150 g of CNT and ultrasonicated for 30 min. The product was then dried overnight at 60 °C oven. After, it was added 1.320 g of $NaH_2PO_2{\cdot}H_2O$ and grinded. The resultant product was submitted to a tubular furnace at 250 °C during 1 h in $N_2$ atmosphere. Afterwards, it was grinded and cleaned with water, 4 to 5 times in a centrifuge at 7600 rpm, rinsed with Ethanol and dried at 60 °C in an oven at ambient pressure.

Figure 10 represents the synthesis procedure for this catalyst. The process was adapted from [37].

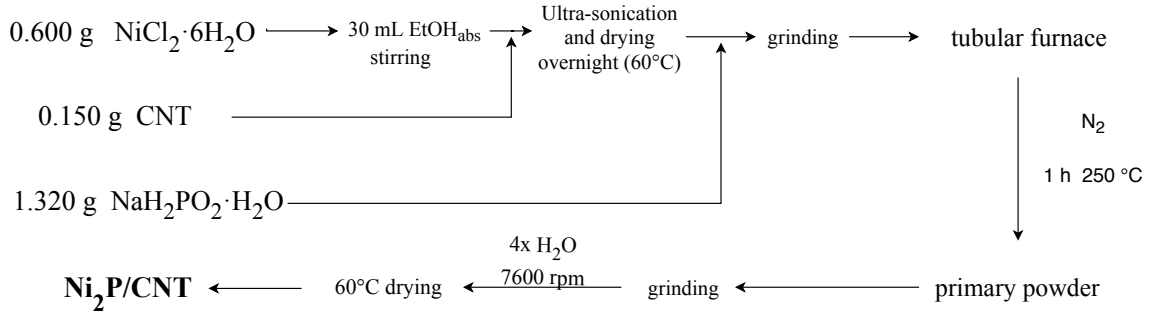



Figure 10: $Ni_2P$/CNT synthesis procedure flowchart.

[5] Merck; EMSURE® ACS,ISO,Reag. Ph Eur Ethanol; 64-17-5

### 3.4.4 $Ni_2P$-Fe/CNT synthesis

For the synthesis of $Ni_2P$-Fe/CNT it was mixed 0.150 g of Fe/CNT, with 0.600 g of $NiCl_2{\cdot}6H_2O$ in 50 ml of Ethanol absolute and sonicated for 30 min. It was then dried in oven at 60 °C at ambient pressure. The product was grinded and added 1.320 g of $NaH_2PO_2{\cdot}H_2O$, for the phosphorization in a tubular furnace for 250 °C for 1 h. Product was then washed in a centrifuge, at 7600 rpm, with $H_2O$ to remove the residues. Rinsed with Ethanol and dried at 60 °C in oven at ambient pressure. Figure 11 present the synthesis procedure for $Ni_2P$-Fe/CNT.

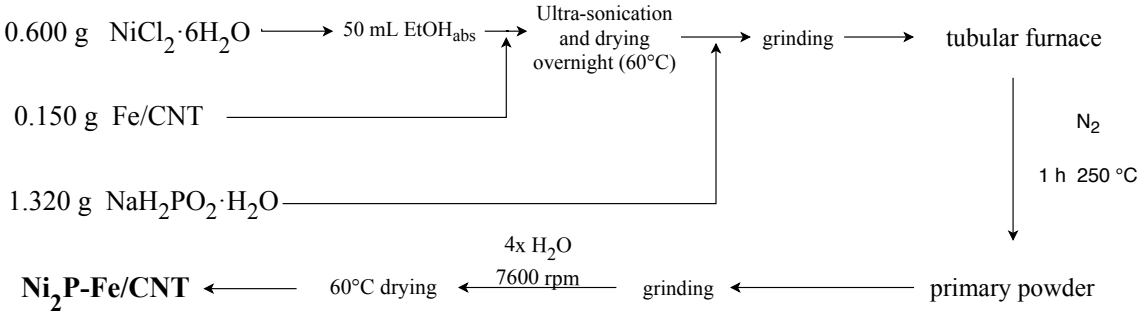



Figure 11: $Ni_2P$-Fe/CNT synthesis procedure flowchart.

### 3.4.5 $Ni_2P$-$Fe_2O_3$/CNT via stirring and ultrassonication

The catalyst $Ni_2P$-$Fe_2O_3$/CNT was synthesized in two different ways. It was first mixed 0.150 g of $Fe_2O_3$/CNT, with 0.600 g of $NiCl_2{\cdot}6H_2O$ in 50 ml of Ethanol absolute.

In the first method, the previous solution was stirred and heated at approximately 100 °C until the ethanol was evaporated. While, in the second method, the previous solution was sonicated for 30 min.

Both catalysts were then dried in oven at 60 °C at ambient pressure, griended after and added 1.320 g of $NaH_2PO_2{\cdot}H_2O$, for the phosphorization in a tubular furnace for 250°C during 1 h. By last, the catalysts were washed in a centrifuge, rotating at 7600 rpm, with $H_2O$ to remove the residues, rinsed with Ethanol and dried at 60 °C in oven at ambient pressure. In figure 12 it is simplified schematically the synthesis procedure for this catalyst.

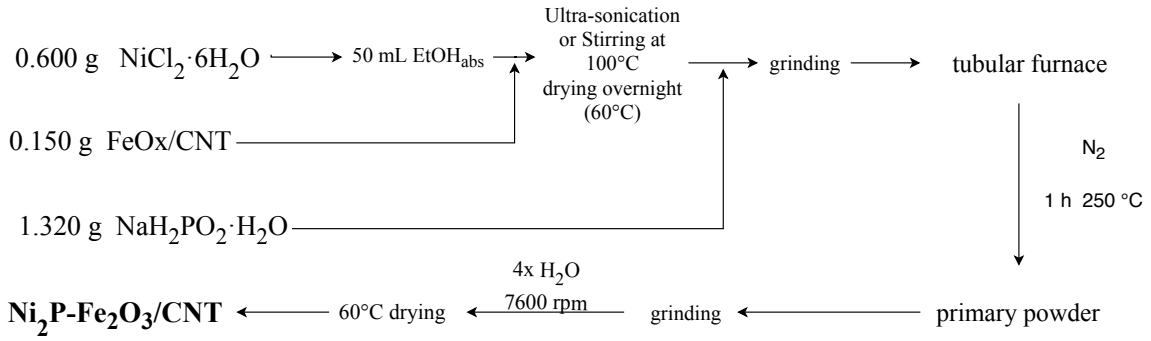



Figure 12: $Ni_2P$-$Fe_2O_3$/CNT synthesis procedure flowchart.

## 3.5 Catalyst ink and layer preparation

To obtain reproducible results in RDE measurements, the first step is to prepare a well-dispersed ink. Before reaching a suitable ink that would fit on the different catalysts, different weight ratios of the components were tested. Catalyst inks were prepared by mixing a solvent, water and in addition an alcohol, isopropanol. To the resulting solution, was then added a binder, a Nafion ionomer. The binder loading affects the catalysts performance, it should be sufficiently high to prevent the electrocatalyst from falling off at high rotation speeds. On the other hand, it could block the access paths of oxygen to the active sites. Therefore, it should be avoided high loading in order to minimize extra diffusion resistance of $O_2$. [3][20] [38]

All of the catalysts inks were prepared with the final composition presented in table 1.

Table 1: Catalyst ink formulation.

| Component | Function | Quantity |
|---|---|---|
| Catalyst | catalyst | 11 mg |
| Ultrapure water[6] | solvent | 2300 µL |
| Isopropanol[7] | solvent | 460 µL |
| Nafion[8] | binder | 45 µL |

Afterwards, the catalyst inks were sonicated in an ice bath for 20 min to make it homogeneous.

[6] Alfa Aesar; Water, ultrapure, HPLC Grade, 7732-18-5
[7] Merck; EMSURE® ACS,ISO,Reag. Ph Eur Ethanol; 64-17-5
[8] Sigma-Aldrich; Nafion® perfluorinated resin solution; 31175-20-9

For all the electrochemical experiments, it was first prepared the glassy carbon electrode (GCE) by polishing it with 0.05 $\mu$m $Al_2O_3$ and then washed using deionized water in sonicater for a few seconds.

Subsequently, it was pipetted 10 $\mu$l of the ink and droped onto the cleaned GCE. The ink dried using the rotational air drying method, which consists in drying under ambient air by rotating the GCE at 700 rpm, which was proved to be the most effective way to fabricate good quality catalyst films, resulting in a better dispersed catalyst film in the GCE leading to higher currents.[39] [20]

The diameter of the GCE used was of 5 mm, hence a surface area of 0.197 $cm^2$. The final catalyst loading is therefore 0.2 $mg\,cm^{-2}$ on the glassy carbon.

# 4 Results

Transition metal phosphides (TMP) have been used to prepare efficient catalysts for OER, displaying a catalytic activity similar to the reference electrodes of iridium black. [40][41] [42][43] In particular, Fe, Ni-based phosphides showed high performance towards OER.[44] Abundance and hence relatively inexpensive makes the TMP-based catalysts quite appealing. In this thesis, phosphides based catalysts, specifically $Ni_2P$ and the support materials, were investigated. Coupling metal nanoparticles with a carbon support material is regarded as an effective strategy for improving catalytic performance. Hence, CNT was used as support and $Ni_2P$/CNT was synthesized and characterized. [45]

$Ni_2P$-$Fe_2O_3$/CNT and $Ni_2P$-Fe/CNT catalysts were idealized, synthesized and characterized (*in situ* and *ex situ*). All of the above catalysts were investigated for ORR and OER performance. These last two are expected to show higher activity because of bimetallic composition. [44] [46] [47]

## 4.1 Electrochemical characterization

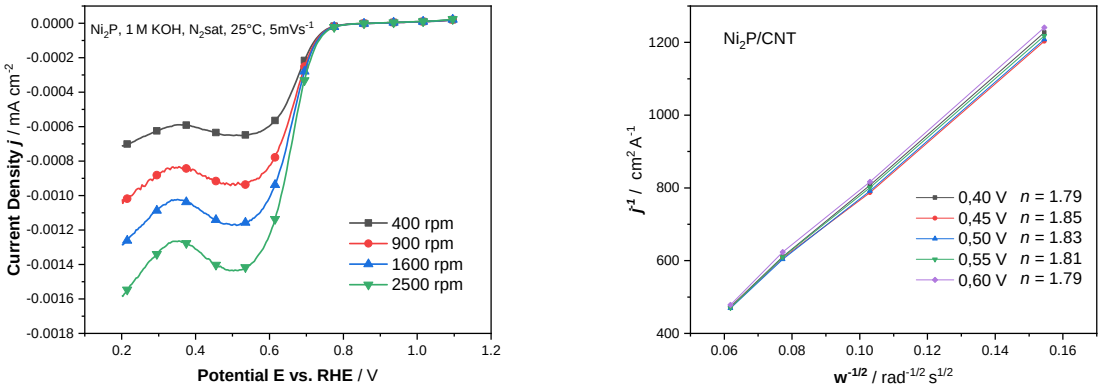
### 4.1.1 ORR activity

The selectivity for the ORR reaction path was studied for each catalyst and compared with Pt/C[9]. For that, LSV experiments at different rotations were carried out. This experiments demonstrate the dependency of the current densities with the rotation speed. K-L plots were obtained, from LSV experiment data, by plotting the inverse of $j$ vs. the inverse of the square root of rotation speed, for different potentials in the diffusion-control region, plot of equation (16). The slope of the K-L plot allowed to calculate $n$ by using equation (17).

In figure 13a and 14a, it is observed that $j_L$ increases with increasing rotation speed, resulting from the higher and faster oxygen flux to the electrode surface. The $E_{\text{onset}}$ does not depend on the rotation speed, being constant throughout the measurements. It is also noted that $Ni_2P$/CNT as a catalysts provides higher current densities than $Ni_2P$.

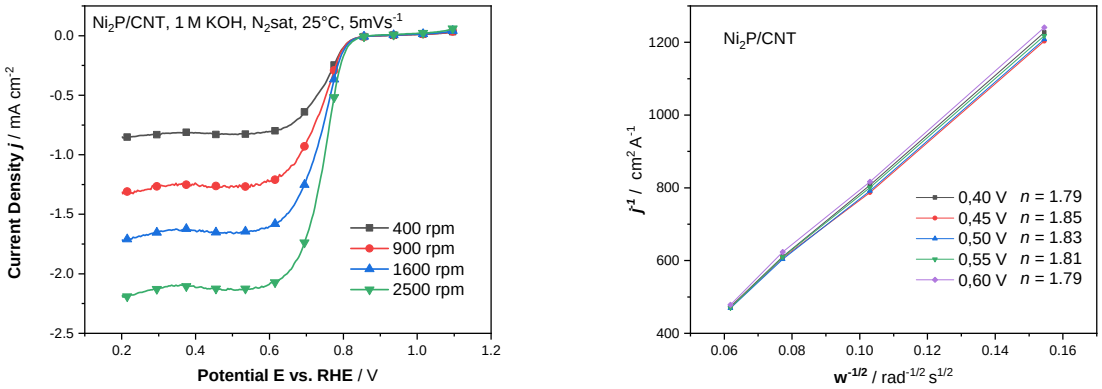
[9] Alfa Aesar; Platinum, nominally 20% on carbon black, HiSPEC® 3000; MFCD00011179

In the K-L plots for $Ni_2P$, figure 13b, and for $Ni_2P$/CNT, figure 14b, one can see that the values of $n$ showed to be around 2 for both catalysts, thereby indicating that the ORR is dominated by the 2 electron pathway, reaction (3). The lines were added for readability.




(a) ORR plot at different rpm (b) K-L plot

Figure 13: $Ni_2P$ ORR activity.

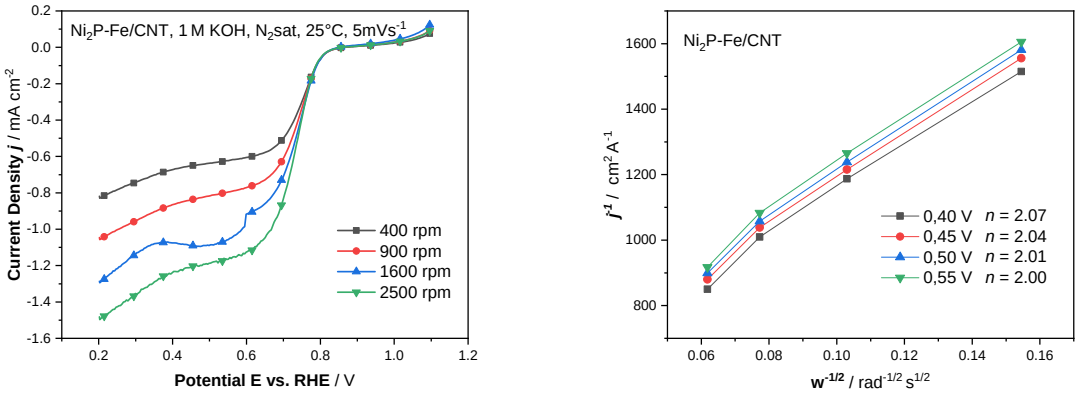



(a) ORR plot at different rpm (b) K-L plot

Figure 14: $Ni_2P$/CNT ORR activity.

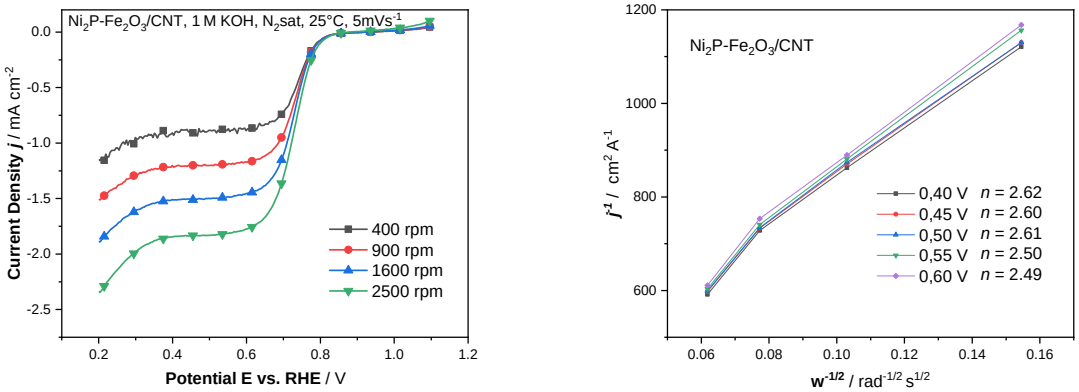
For $Ni_2P$-Fe/CNT, figure 15a, and for $Ni_2P$-$Fe_2O_3$/CNT, figure 16a, the results obtained were similar to the ones obtained for the previous catalysts. The $j_L$ increased with increasing rotation speed, being the highest for 2500 rpm. $Ni_2P$-$Fe_2O_3$/CNT reached higher currents compared with $Ni_2P$-Fe/CNT. On the other hand, the currents of $Ni_2P$-$Fe_2O_3$/CNT are similar to the ones obtained for $Ni_2P$/CNT, while the currents of $Ni_2P$-Fe/CNT are similar to $Ni_2P$.

Both of these catalysts follow the 2 electron pathway for the ORR reaction, as the $n$ calculated for both was around 2, presented in figures 15b and 16b.




(a) ORR plot at different rpm (b) K-L plot

Figure 15: $Ni_2P$/Fe/CNT ORR activity.




(a) ORR plot at different rpm (b) K-L plot

Figure 16: $Ni_2P$-$Fe_2O_3$/CNT ORR activity.

In summary, all the synthesized catalysts follow the 2 electron pathway for ORR, reaction 3. On the other hand, Pt/C was proved to follow the 4 electron pathway reaction (equation 2) which highly preferential as it was previously explained.[Consult figure 36 in Appendix A.1]

For an overall performance understanding, the ORR activities of the catalysts were compared at a constant 1600 rpm in the potential window between 0.2 V and 1.1 V, figure 17.

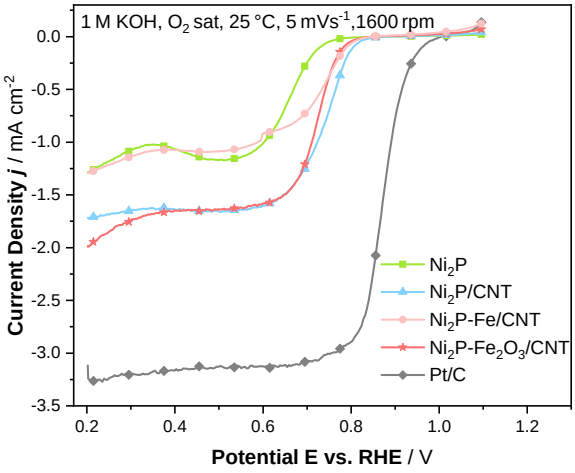



Figure 17: ORR activity

As it can be seen in the above graph 17, the addition of the CNT support in $Ni_2P$ not only resulted in a better $E_{\text{onset}}$ but also in a higher $j_L$. A similar performance was noted for the addition of $Fe_2O_3$, while using Fe supported on CNT does not increase the activity of $Ni_2P$, however has a better $E_{\text{onset}}$. Even though using different approaches made possible the increase of $Ni_2P$ performance, it can be easily concluded that the ORR activity of none of the synthesized catalysts are comparable to Pt/C.

Taking into account the results obtained in the K-L plots, it is possible to understand, and explain, the noticeable difference between the current densities reached in Pt/C and all of the $Ni_2P$ based catalysts.

The different $E_{\text{onset}}$, $E_{1/2}$ and $j_L$ values, from plot 17, can be compared in table 2.

Table 2: ORR parameters.

| **Catalyst** | $\boldsymbol{j}_{\mathrm{L}}$ | $\boldsymbol{E}_{1/2}$ | $\boldsymbol{E}_{\mathrm{onset}}$ |
|---|---|---|---|
| | mA cm$^{-2}$ | V | V |
| Pt/C | 3.25 | 0.87 | 0.92 |
| $Ni_2P$ | 1.25 | 0.65 | 0.72 |
| $Ni_2P$/CNT | 1.75 | 0.74 | 0.80 |
| $Ni_2P$-Fe/CNT | 1.25 | 0.70 | 0.77 |
| $Ni_2P$-$Fe_2O_3$/CNT | 1.75 | 0.71 | 0.77 |

For the synthesized catalysts, it can be seen from table 2, that the $E_{\mathrm{onset}}$ has the highest value for $Ni_2P$/CNT, nonetheless both catalysts with Fe/CNT and $Fe_2O_3$/CNT present better value than $Ni_2P$. The highest value of $E_{1/2}$ and $j_L$ are for the $Ni_2P$/CNT and $Ni_2P$-$Fe_2O_3$/CNT.

### 4.1.2 OER activity and Tafel plot

OER activity tests for all the catalysts, including Ir Black[10] as benchmark were tested. The OER plot (iR- corrected) is showed in figure 18. The ohmic resistance can be determined by performing an Electrochemical Impedance Spectroscopy (EIS) test [amplitude of 10 mA with frequencies from 100 kHz to 500 mHz]. The OER curves were plotted with an associated error. The error bars were calculated by doing the mean of 3 measurements. For the positive error it was subtracted the maximum value of the 3 measurements to the mean value and for the negative error it was subtracted the minimum value of the 3.

[10] Umicore, Iridium Black, 99% purity, 7439-88-5

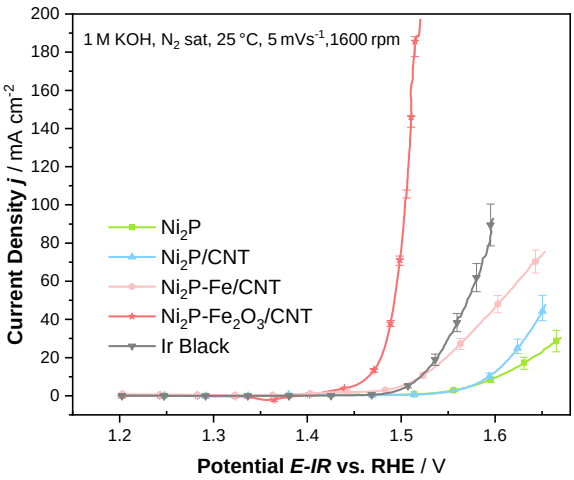
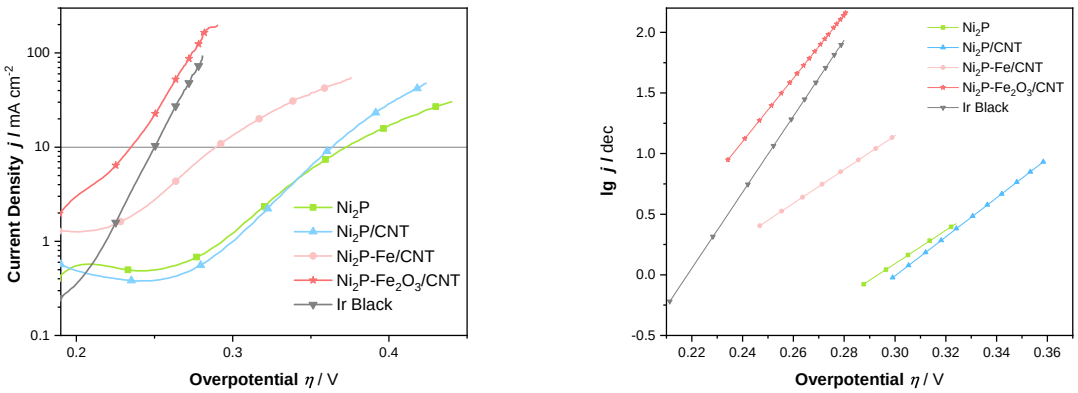



Figure 18: OER activity

Among all the materials, $Ni_2P$ demonstrated the most sluggish OER performance and $Ni_2P$-$Fe_2O_3$/CNT shows an outstanding activity relative to other catalysts, including Ir Black. It can also be seen that the presence of CNT might be the reason why conductivity of the materials is increased resulting in higher currents. Nonetheless, the effect on the surface could also be a possible explanation. However the $E_{\text{onset}}$ remained the same for $Ni_2P$ and $Ni_2P$/CNT. $E_{\text{onset}}$ has been found relatively lower for $Ni_2P$-Fe/CNT and $Ni_2P$-$Fe_2O_3$/CNT when compared to other catalysts, this phenomena could be attributed to the presence of Fe in these materials. The reason for enhanced OER performance in existence of Fe could be associated with the increase in the surface area or even the synergistic effect of Fe on Ni ultimately improving OER activity. [45] The $E_{\text{onset}}$ from the catalysts in plot 18 are presented in table 3.

From the Tafel plot, it is possible to obtain the Tafel slope, which is an important kinetic parameter to investigate the OER kinetics, as was previously mentioned. The $\eta$ was calculated by subtracting the applied potential to the theoretical potential required to start the OER reaction, 1.23 V vs. RHE. Tafel plot of all the catalysts is presented in figure 19a.

For the Tafel slopes calculation it was made a linear regression in the range where the reaction occurs for each catalyst. The individual ranges used for the fitting analyses of each catalyst is presented in figure 19b.




(a) Tafel Plot

(b) Tafel slopes

Figure 19: Evaluation of OER activity.

However, to fully determine the catalytic behaviour there is need to define other parameters because $B$ does not present the complete picture itself. Possible parameters that can be used in combination with $B$ are $j_0$ and $\eta$ at a defined $j$. Normally, $\eta$ is taken at $10\,\mathrm{mA\,cm^{-2}}$ , $\eta_{10}$ . [45] The values obtained from Tafel plot including Tafel slope $B$, $\eta_{10}$ and $j_0$ are presented in table 3.

Table 3: Tafel equation parameters.

| **Catalyst** | $\boldsymbol{B}$ | $\boldsymbol{j_0}$ | $\boldsymbol{\eta}$ @10 mA/cm$^2$ | $\boldsymbol{E}_{\mathrm{onset}}$ |
|---|---|---|---|---|
| | mV dec$^{-1}$ | mA cm$^{-2}$ | mV | V |
| Ir Black | 32 | 1.42x10$^{-7}$ | 250 | 1.52 |
| $Ni_2P$ | 73 | 9.24x10$^{-5}$ | 373 | 1.57 |
| $Ni_2P$/CNT | 62 | 1.44 x10$^{-5}$ | 364 | 1.57 |
| $Ni_2P$-Fe/CNT | 72 | 9.33x10$^{-4}$ | 290 | 1.52 |
| $Ni_2P$-$Fe_2O_3$/CNT | 37 | 3.90x10$^{-6}$ | 236 | 1.48 |

As one can see from the table, $Ni_2P$ has the highest $B$, and comparable to $Ni_2P$-Fe/CNT, the highest value for $\eta_{10}$ as well as the highest value for $E_{\mathrm{onset}}$, which is the same as $Ni_2P$/CNT. However, this last catalysts presents a much better $B$, even though the $\eta_{10}$ is also a high value. Introducing Fe into the catalysts leads to a high decrease in the $\eta_{10}$ as well as in the $E_{\mathrm{onset}}$. $Ni_2P$-$Fe_2O_3$/CNT presents the lowest $E_{\mathrm{onset}}$, even when compared to the benchmark catalyst,

and also a comparable $B$, which can be the reason it leads to increase in OER activity for this catalyst.

Furthermore, a high $j_0$ is a good indicator of a good electrocatalyst for the reaction since it provides an idea of the catalyst activity without the effect of the surface area. However, determining $j_0$ could lead in error because a very small error in determining $B$, e.g. derived from the linear fitting, can lead to large difference in the values. [45] Ir Black is the catalyst which presents the worst $j_0$ meaning that the catalytic activity of this catalyst is not desirable. On the other hand, $Ni_2P$-Fe/CNT presents the best value of $j_0$.

Regarding $\eta_{10}$, $Ni_2P$-$Fe_2O_3$/CNT presented the lowest value, 236 mV, surpassing the value of Ir Black for the same parameter, 250 mV.

### 4.1.3 Capacitance measurements

The electrochemical double layer capacitance ($c_{dl}$) is important to compare the intrinsic activity of catalyst materials. The $c_{dl}$ of catalyst $Ni_2P$-$Fe_2O_3$/CNT was the highest which elucidates that this catalyst might have a higher electrochemically active surface area (ECSA)

It is also noticeable that the addition of CNT to $Ni_2P$ leads to a great increase in the $c_{dl}$ by 10 times. On the other hand, the addition Fe/CNT increases the $c_{dl}$ value relatively to $Ni_2P$ but decreases in comparison with $Ni_2P$/CNT. The low activity of $Ni_2P$ when compared with the other catalysts, might be due to the low value for ECSA that this catalyst shows. Even though, Ir Black showed a higher $c_{dl}$ value, $Ni_2P$-$Fe_2O_3$/CNT still presented higher current densities regarding the OER. The $c_{dl}$ values are presented in table 4.

Table 4: Capacitance values measured for all catalysts.

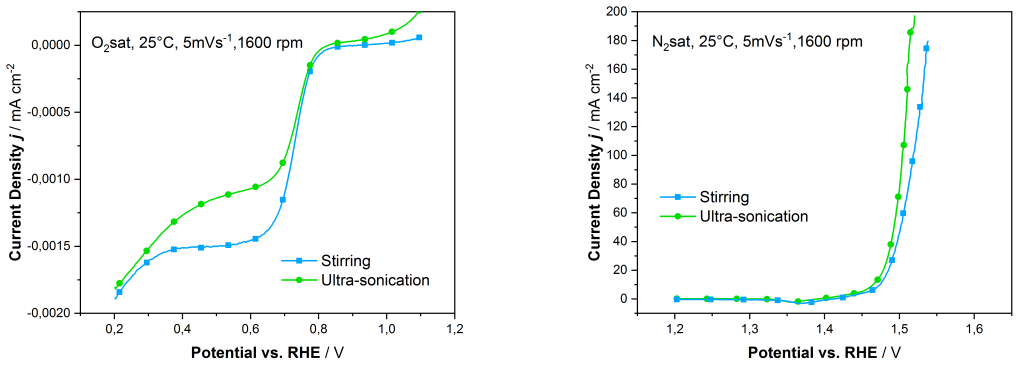
| **Catalyst** | Ir Black | $Ni_2P$ | $Ni_2P$/CNT | $Ni_2P$-Fe/CNT | $Ni_2P$-$Fe_2O_3$/CNT |
|---|---|---|---|---|---|
| $\boldsymbol{c}_{dl}$ (μF $cm^{-2}$) | 3500 | 90 | 900 | 700 | 1100 |

For more information regarding this measurement and calculations performed consult Annex A.1, figure 39.

## 4.2 Ultra-sonication vs. stirring for $Ni_2P$-$Fe_2O_3$/CNT

As it was mention in chapter *3.4 Catalyst synthesis*, $Ni_2P$-$Fe_2O_3$/CNT was synthesized with two different methods, to understand which method provides a better catalytic performance. Catalysts were characterized electrochemically and physically.

Figure 20 shows ORR (20a) and OER (20b) activity for the different synthesis procedures. Regarding ORR reaction both methods provide the same $E_{\text{onset}}$, nonetheless stirring provides a better $j$ and $E_{1/2}$. As for the OER, the $E_{\text{onset}}$ , is practically the same however the $j$ is higher ultra-sonication method. The ORR and OER plot are presented in figure 20.




(a) ORR (b) OER

Figure 20: Electrochemical characterization of $Ni_2P$-$Fe_2O_3$/CNT via ultra-sonication and stirring

To further understand the behaviour of catalysts obtained from different synthesis process (ultra-sonication and stirring), it was plotted the Tafel plot, figure 21. The parameteres obtained from the tafel plot, such as $B$, $j_0$ and $\eta_{10}$ are present in table 5.

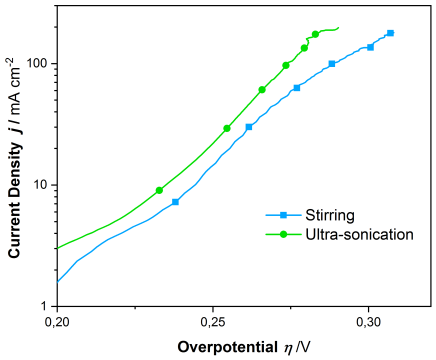



Figure 21: Tafel plot of $Ni_2P$-$Fe_2O_3$/CNT via stirring and ultra-sonication.

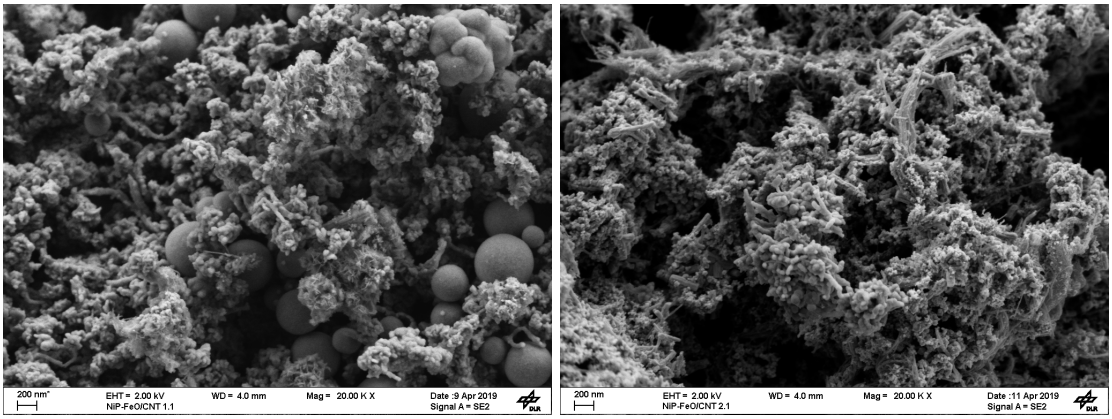
Table 5: Tafel plot parameters of $Ni_2P$-$Fe_2O_3$/CNT via stirring and ultra-sonication.

| **Process** | $B$ | $j_0$ | $\eta$**@10 mA cm$^{-2}$** |
|---|---|---|---|
| | mV dec$^{-1}$ | mA cm$^{-2}$ | mV |
| Stirring | 37 | 3.31x10$^{-6}$ | 240 |
| Ultra-sonication | 38 | 3.90x10$^{-6}$ | 236 |

From table 5, The Tafel slopes obtained were quite identical as well as $j_0$. The $\eta_{10}$ values are also quite similar, nonetheless ultra-sonication process is found to be slightly better than stirring.

The $c_{dl}$ measurements, also shows significant difference between processes. The $c_{dl}$ of the catalyst $Ni_2P$-$Fe_2O_3$/CNT prepared with ultra-sonication is found to be 1100 µF cm$^{-2}$, while for stirring the value is much lower, 600 µF cm$^{-2}$. This values indicates that there is a significant difference in ECSA of the catalysts prepared using different synthesis route, namely ultra-sonication is better than stirring.

The above observation about catalyst prepared via ultra-sonication route can be supported by SEM images, figure 22b, shows more homogeneous structure along with evenly dispersed particles. For instance spherical agglomerates at figure 22a, possible NiOx, seemed to be dispersed by the usage of ultra-sonication.




(a) Preparation via stirring (b) Preparation via ultra-sonication

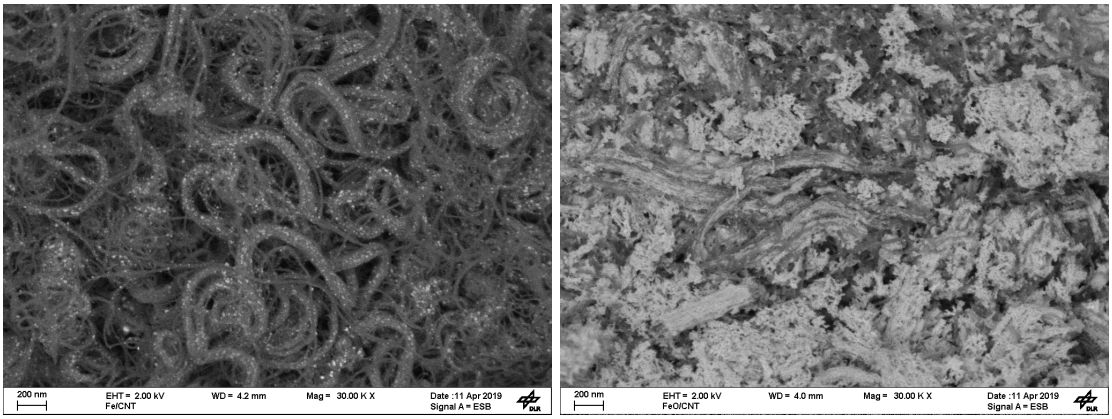
Figure 22: SEM images for $Ni_2P$-$Fe_2O_3$/CNT, SE

Taking all of the above results in consideration, it can be established that ultra-sonication is better of the two routes to synthesize the catalyst.

## 4.3 Physical characterization

### 4.3.1 SEM Results

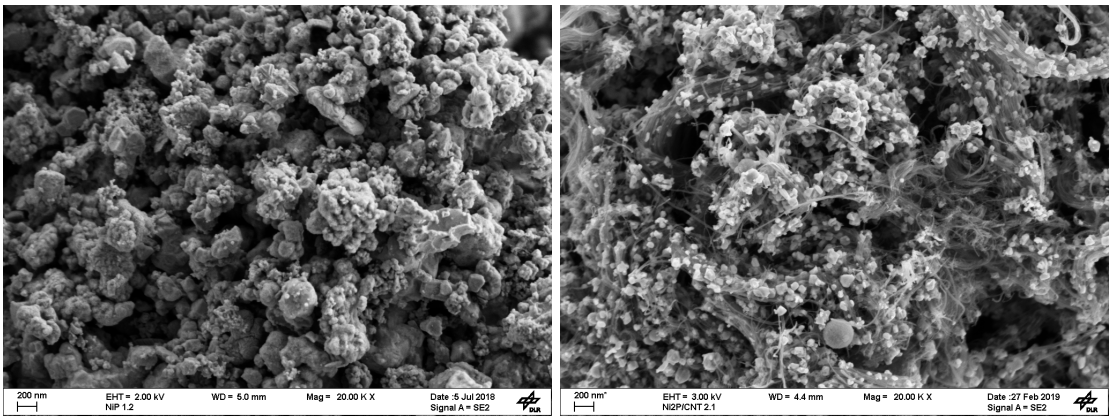
To have access to the morphology of the catalyst, SEM images of two synthesized Fe and $Fe_2O_3$ supported on CNT catalysts were obtained. The SEM images presented in figure 23 were obtained in ESB to show better contrast between Fe/$Fe_2O_3$ and CNT. In figure 23a, the Fe particles (bright nanosized particles) show a well dispersion on CNT surface (dark tubes), while in figure 23b the $Fe_2O_3$ particles (white parts) seem to be agglomerated, originating big cluster of particles on CNT. The SEM images also suggest that the Fe content seems to be lower in Fe/CNT than in $Fe_2O_3$/CNT. The EDX analysis in Appendix A.1, table 11 and 12, indicates a lower ratio content of Fe/C in Fe/CNT than in $Fe_2O_3$/CNT, agreeing with the SEM pictures.




(a) Fe/CNT (b) $Fe_2O_3$/CNT

Figure 23: SEM images, ESB

SEM images were obtained for accessing the porosity and morphology of the catalysts $Ni_2P$, figure 24a, and $Ni_2P$/CNT, figure 24b. The later catalyst apparently looks to have bigger pores and uniform dispersion of $Ni_2P$ on CNT as well as less agglomeration of particles comparatively to $Ni_2P$. This two characteristics might provide a higher surface area and ultimately more electrochemical active sites for ORR and OER.



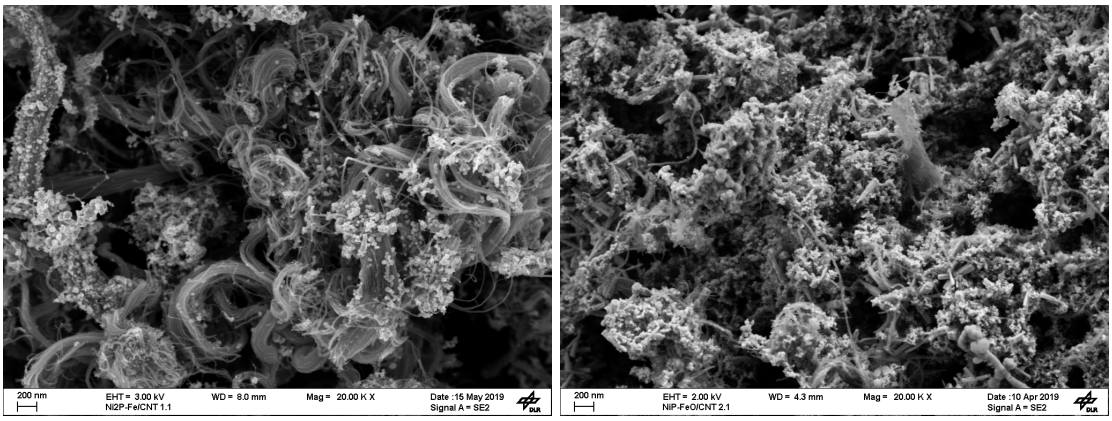

(a) $Ni_2P$ (b) $Ni_2P$/CNT

Figure 24: SEM images of $Ni_2P$ and $Ni_2P$/CNT, SE

In figure 25a, it is clear the dispersion of the catalysts on CNT with porous morphology, even though the pores and pore sizes are unevenly distributed. However, the dispersion of $Ni_2P$-Fe is non homogeneous with some agglomerations.

Figure 25b, the catalyst shows porous structure, with surface of CNT well covered with $Ni_2P$

and $Fe_2O_3$ creating a arrangement of interconnected particles.




(a) $Ni_2P$-Fe/CNT (b) $Ni_2P$-$Fe_2O_3$/CNT

Figure 25: SEM images of Fe based catalysts, SE

Having compared all of the four catalysts it looks like $Ni_2P$-$Fe_2O_3$/CNT presents a higher dispersion of particles and hence might present a higher catalyst surface area. These results are in agreement with $C_{dl}$ measurement, which proves that $Ni_2P$-$Fe_2O_3$/CNT could have a higher ECSA in comparison with the other synthesized catalysts. All of the above mentioned characteristics might be the reason why this catalyst has superior catalytic activity towards OER.

It is important to note that all SEM images are taken at selective regions and for that they are not representative of the whole powder, giving simply a clue of what the catalyst might be like.

### 4.3.2 EDX Results

The EDX analysis, table 6 suggests a homogeneous Ni/P molar ratio to be approximately 2:1. The carbon and oxygen shown in EDX can arise from impurities (contamination from the atmosphere) in the material or from measurements errors (the carbon tape used for EDX). The areas chosen to characterization are represented in figure 26.

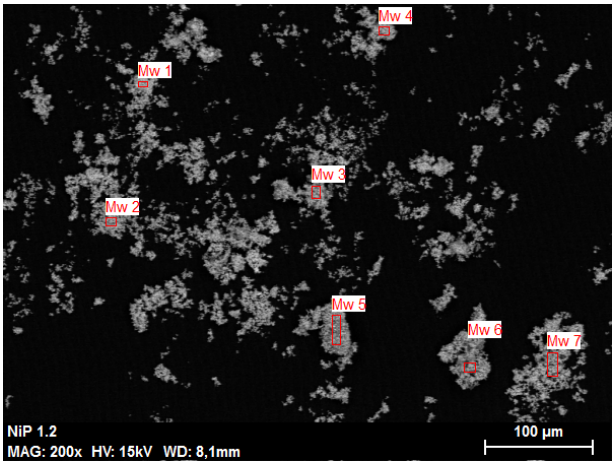



Figure 26: $Ni_2P$ EDX

Table 6: Mass fraction % spectrum of $Ni_2P$

| **Spectrum**wt% | **C** | **O** | **P** | **Ni** |
|---|---|---|---|---|
| Mw 1 | 10.49 | 4.47 | 18.41 | 66.64 |
| Mw 2 | 7.11 | 3.68 | 17.93 | 71.29 |
| Mw 3 | 11.54 | 3.41 | 17.05 | 67.99 |
| Mw 4 | 12.07 | 4.07 | 17.46 | 62.80 |
| Mw 5 | 11.60 | 8.29 | 17.31 | 62.80 |
| Mw 6 | 11.02 | 2.09 | 18.14 | 68.74 |
| Mw 7 | 8.81 | 2.97 | 18.23 | 69.99 |

As for $Ni_2P$/CNT it is observed, in figure 27 and table 7, that average mass fraction of C is around 60%, though the distribution of C was found to be non-homogeneous. The compositions along the different areas also indicat the non uniform distribution of the $Ni_2P$ on the CNT. Sodium comes as an impurities coming from $Ni_2P$ phosphorizing agent ($NaH_2PO_2 \cdot H_2O$) which was not removed completely during the cleaning step. In addition, Sulfur was also observed in EDX as an impurity and it is important to take in consideration that it can be responsible for poisoning the catalyst by blocking the active sites. Nonetheless, the quantity of Sulfur appears to be very low to cause a serious effect on the catalyst activity.

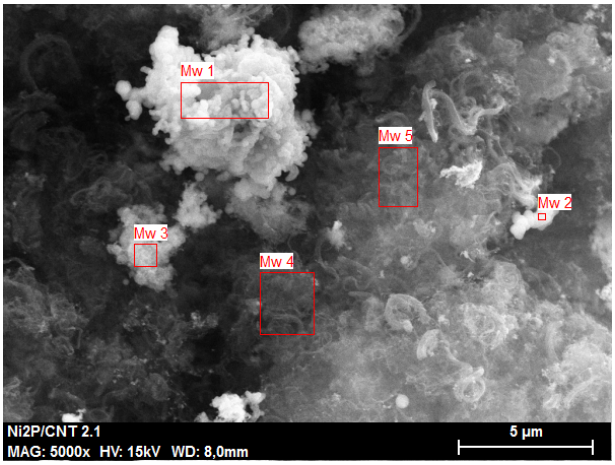



Figure 27: $Ni_2P$/CNT EDX

Table 7: Mass fraction % spectrum of $Ni_2P$/CNT

| Spectrum wt% | C | O | Na | P | S | Ni |
|---|---|---|---|---|---|---|
| Mw 1 | 33.00 | 36.01 | 0.37 | 8.26 | - | 22.35 |
| Mw 2 | 45.18 | 32.98 | 0.29 | 5.05 | - | 16.50 |
| Mw 3 | 59.82 | 22.54 | 0.41 | 3.78 | 0.29 | 13.16 |
| Mw 4 | 83.76 | 5.73 | - | 2.46 | 0.39 | 7.67 |
| Mw 5 | 82.11 | 6.06 | 0.15 | 1.95 | 0.24 | 9.48 |

As one can see $Ni_2P$-Fe/CNT, figure 28 and table 8, show that the amount of Fe is quite low. This can be related to the less quantity of Fe on the synthesized Fe/CNT [figure 38 and table 12 present in Appendix A.1] as well as a result of metal losses in the cleaning procedure after synthesis. The wide range of the elements mass% composition indicate a non-homogeneous composition of the catalyst.

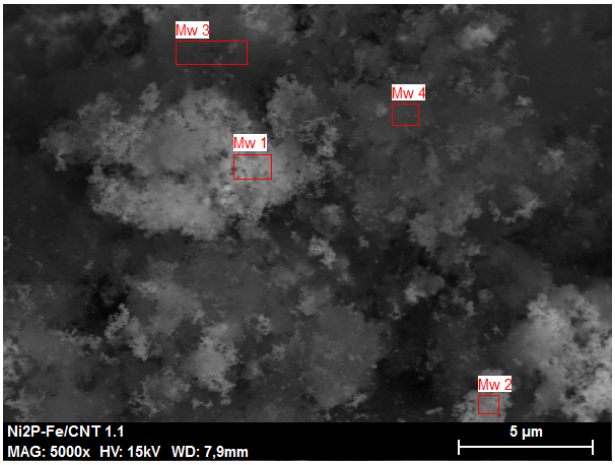



Figure 28: $Ni_2P$-Fe/CNT EDX

Table 8: Mass fraction % spectrum of $Ni_2P$-Fe/CNT

| **Spectrum** wt% | **C** | **O** | **P** | **Fe** | **Ni** |
|---|---|---|---|---|---|
| Mw 1 | 39.50 | 5.04 | 12.13 | 3.61 | 39.72 |
| Mw 2 | 42.15 | 6.44 | 12.52 | 3.22 | 35.67 |
| Mw 3 | 61.32 | 7.65 | 7.56 | 3.55 | 19.93 |
| Mw 4 | 64.38 | 10.17 | 7.31 | 2.91 | 15.23 |

In figure 29 are represented the respective areas chosen for characterization and table 9 present the EDX analysis for $Ni_2P$-$Fe_2O_3$/CNT. When compared to $Ni_2P$-Fe/CNT the amount of C is found to be lower, while the amount of Fe is found to be higher. This is in agreement with the SEM pictures, for Fe-CNT and $Fe_2O_3$-CNT, in which is possible to see that the content of Fe is lower in the first catalyst when compared to the second one.

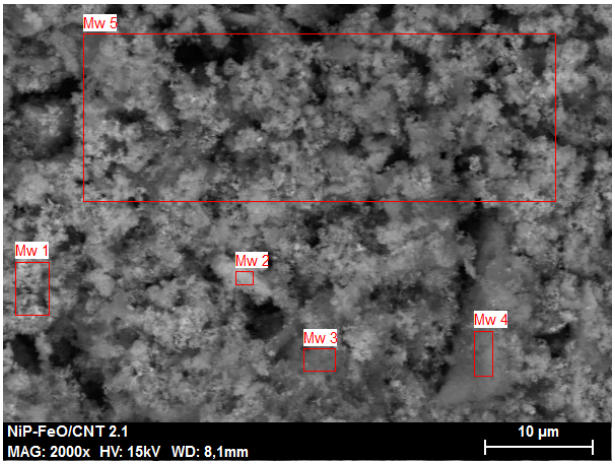



Figure 29: $Ni_2P$-$Fe_2O_3$/CNT EDX

Table 9: Mass fraction % spectrum of $Ni_2P$-$Fe_2O_3$/CNT

| **Spectrum wt%** | **C** | **O** | **P** | **Fe** | **Ni** |
|---|---|---|---|---|---|
| Mw 1 | 19.94 | 5.06 | 20.79 | 19.86 | 34.35 |
| Mw 2 | 17.38 | 9.26 | 19.08 | 10.24 | 44.03 |
| Mw 3 | 37.34 | 15.54 | 17.30 | 14.86 | 14.97 |
| Mw 4 | 26.68 | 15.85 | 19.06 | 15.38 | 23.03 |
| Mw 5 | 12.50 | 14.77 | 19.99 | 17.95 | 34.80 |

The designed composition of $Fe_2O_3$/CNT and Fe/CNT before synthesis was 30% mass fraction of Fe/$Fe_2O_3$ and 70% mass fraction of CNT. However, in the synthesized material Fe particles

in the support is around 32% and O 23% while the C correspond to around 42% mass fraction for $Fe_2O_3$/CNT. In Appendix A.1, table 11 and table 12is presented the EDX composition for both catalysts.

For the Fe/CNT the mass fraction composition of Fe is a little lower (12%) than the one calculated for catalyst synthesis (30%), indicating that not all Fe was reduced after synthesis and still some O particles might have oxidized the Fe.

Regarding the EDX measurements, it should be taken in consideration that only small sections are analysed and are not representative of the whole catalyst.

### 4.3.3 XRD Results

In Figure 30, is shown the XRD of $Ni_2P$ and $Ni_2P$/CNT. The measurements were done with Cu-Kα x-ray source and plotted together. It is clearly seen the peaks of $Ni_2P$ for 2-Theta angles higher than 40°. The graphite peak, assigned to the CNT, is evident in the $Ni_2P$/CNT catalyst, for Theta angles in the range of 24°to 27°.

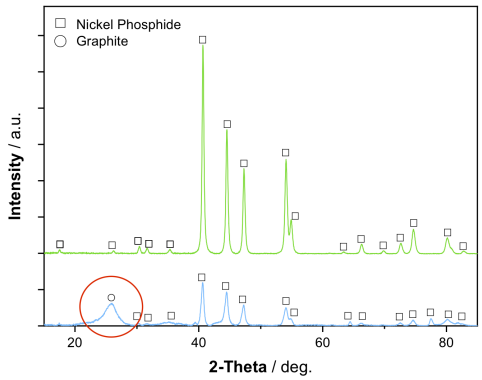



Figure 30: $Ni_2P$ and $Ni_2P$/CNT XRD

XRD with Co x-ray source was done for the catalysts with Fe content. Figure 31, presents the results obtained for $Fe_2O_3$/CNT, $Ni_2P$-$Fe_2O_3$/CNT, Fe/CNT and $Ni_2P$-Fe/CNT.

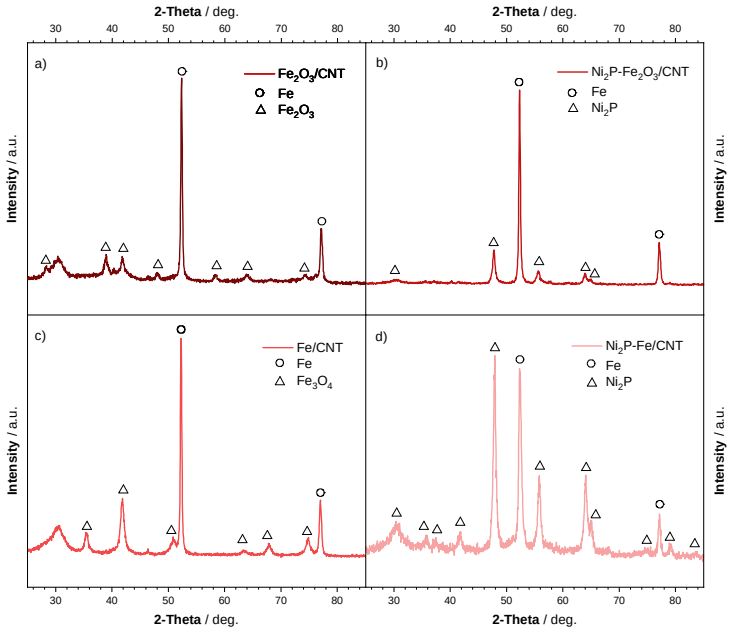



Figure 31: XRD graphs for a) $Fe_2O_3$/CNT, b) $Ni_2P$-$Fe_2O_3$/CNT, c) Fe/CNT and d) $Ni_2P$-Fe/CNT.

The common Fe peak for all the catalysts is related to the sample holder and not to the catalyst itself. $Fe_2O_3$/CNT was synthesized successfully since it presents the peaks for the specific iron oxide intended. However, the last catalyst, $Ni_2P$-$Fe_2O_3$/CNT, did not display the characteristic peaks of $Fe_2O_3$. This indicates that the the amount of $Fe_2O_3$ can be really small or even nonexistent. The peaks, even though small, only seemed to match the $Ni_2P$ database.

On the other hand, Fe/CNT was not synthesised with success since it not presented Fe peaks that correspond to the catalyst, but only to the sample holder. It presented instead peaks that meet the database for $Fe_3O_4$. Furthermore, $Ni_2P$-Fe/CNT was not synthesised with success, it did not appear not only Fe peaks nor $Fe_3O_4$, which once more this last one could be present in really small amounts and not detectable by the XRD, which only detected $Ni_2P$ peaks with higher intensity.

### 4.3.4 XPS Results

In order to trace Fe, XPS measurements were conducted for the catalysts: $Ni_2P$, $Ni_2P$-$Fe_2O_3$/CNT and $Ni_2P$-Fe/CNT. It was tested for the Ni2p, Fe2p and P2p binding energy regions and the results are, respectively, presented in figure 32.

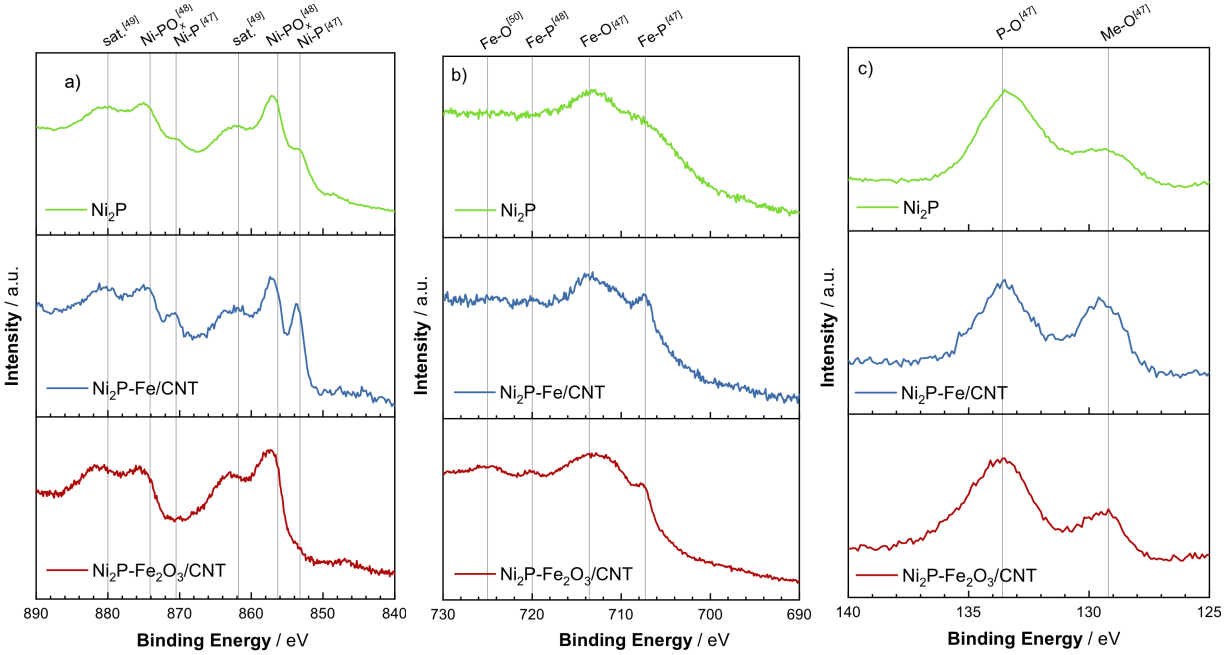



Figure 32: XPS spectra of a) Ni 2p, b) Fe 2p and c) P 2p regions, respectively.

In the Ni2p spectrum the peaks at 870.5 eV and 853.2 eV are assigned to the binding energies of Ni 2p1/2 and Ni 2p3/2 for Ni-P group [48], while the peaks located at 874.1 eV and 856.3 eV are coherent with the binding energy of Ni 2p1/2 and Ni 2p3/2 for Ni-$PO_x$. [49] The peaks at 880 eV and 861.8 eV are owing to Ni satellite (sat.) peaks. [50]

In the spectrum of Fe2p, the peaks located at 720 eV and 707.3 eV can be regarded as Fe-P[49] [48] and the others at 725.6 eV and 713.6 eV could lead to Fe oxide species[51][48]. At 713.6 eV is also common the Ni Auger peak, which was possible added to the Fe-O peak at the same region, explaining why there is a peak in $Ni_2P$.

The P2p spectrum can be fitted into two 2 peaks. The peak corresponding to P-O at 133.6 eV [48] and the oxidized metal phosphate species peak, Me-P at 129.2 eV [48]. Me can be Ni and Fe. [48]

Fe may have replace Ni in the phoshorization process giving rise to FeP. Ni and Fe have similar atomic radii, hence Fe can be incorporated into $Ni_2P$ lattice without noticeable deformation. This can also explain the absence of Fe oxides in the XRD results. The catalyst synthesized might be NiFeP with undefined atomic ratio denoted by $Ni_{2-x}Fe_xP$.

### 4.3.5 TGA Results

In the TGA measurement for the catalyst $Ni_2P$/CNT, figure 33, it is clear the ratio difference between $Ni_2P$ and CNT. The plot shows, in the beginning, a small decrease ( 4.59%) in the mass which could be related to evaporation of water in the pores as well as other volatile components. At around 600 °C, there is a considerable decrease in the mass % of the catalyst which is related to the CNT burn. [Consult figure 40, present in Appendix A.1] It is possible to affirm that this catalyst is composed by 58% $Ni_2P$ and 42% CNT.

The TGA measurements regarding $Ni_2P$-$Fe_2O_3$/CNT and $Ni_2P$-Fe/CNT catalysts are shown in Appendix A.1 figures 41a and 41b. They are not reliable since, despite the use of an argon atmosphere, the mass increased; this was assigned to an experimental error. Since the measurements from these catalysts were not reliable and it is not possible to predict the content of CNT in the catalysts, it was measured Fe/CNT and $Fe_2O_3$/CNT, figures 34 and 35, to estimate the compositions. TGA analysis shows higher content of CNT for Fe/CNT (66%) than $Fe_2O_3$/CNT (35%), as it was apparent in SEM image 23a and 23. The different amount of support will have consequent effect on the final mass fraction of CNT in the final correspondent catalysts, $Ni_2P$-$Fe_2O_3$/CNT and $Ni_2P$-Fe/CNT.

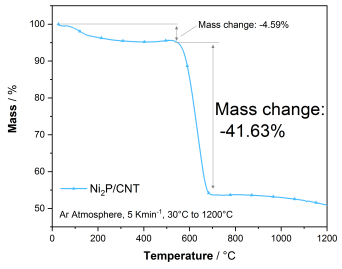



Figure 33: $Ni_2P$/CNT TGA

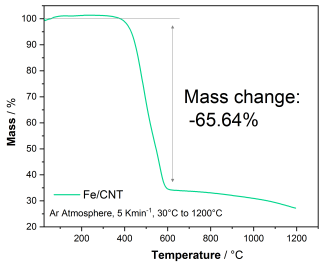



Figure 34: Fe/CNT TGA

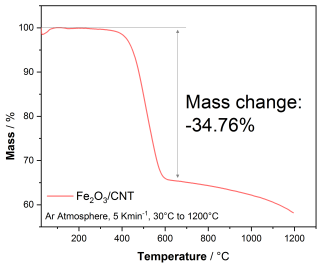



Figure 35: $Fe_2O_3$/CNT

### 4.3.6 BET Results

BET surface area measure the surface area available providing an upper bound to the active surface area (which is commonly lower than the total surface area). For $Ni_2P$ the BET value measured was $1\,m^2\,g^{-1}$ it can be considered that the specific surface area (SSA) for this catalyst is really low, when compared to the other catalysts. $Ni_2P$/CNT presented a SSA of $120\,m^2\,g^{-1}$, the highest of all the catalysts, since this catalyst has a higher CNT content (42%) in comparison with $Ni_2P$-$Fe_2O_3$/CNT and $Ni_2P$-Fe/CNT which have a SSA of $70\,m^2\,g^{-1}$ and $73\,m^2\,g^{-1}$, respectively. It is possible to assume that only CNT is contributing to the increase on SSA. Considering the TGA measurements it is possible to understand that there is less content of CNT in $Ni_2P$-Fe/CNT and even less on $Ni_2P$-$Fe_2O_3$/CNT, since Fe/CNT TGA measurement showed CNT content of 66% and $Fe_2O_3$/CNT showed an even lower number 35%, which is reflected on the final catalyst CNT content. It can be concluded that the support gives a better dispersion of the catalyst providing a higher surface area.

The $c_{dl}$ values reported before, $\mu F\ cm^{-2}$, were converted to $m^2\,g^{-1}$ for a direct comparison with BET results. The ECSA values were calculated by dividing $c_{dl}$ values by a specific capacitance of 40 $\mu F\ cm^{-2}$ , typical value used, and by the catalyst loading in RDE, $0.2\,mg\,cm^{-2}$. [52] Using ECSA and BET surface areas provides a limiting range of specific activities allowing to better compare the performance of catalysts.[52] In table 10 it is presented the comparison between both measurements.

Table 10: BET and ECSA values obtained.

| Catalyst | **$Ni_2P$** | **$Ni_2P$/CNT** | **$Ni_2P$-Fe/CNT** | **$Ni_2P$-$Fe_2O_3$/CNT** |
|---|---|---|---|---|
| **BET** $m^2\,g^{-1}$ | 1 | 120 | 73 | 70 |
| **ECSA** $m^2\,g^{-1}$ | 1.1 | 11.3 | 8.8 | 13.8 |

No obvious correlation between BET surface areas measured and ECSA. Except for $Ni_2P$, which yield similar results for the BET and ECSA. The low surface area and low catalytic active surface area is reflected on the low current densities of $Ni_2P$. Nevertheless, it appears that the effect of the surface area is negligible on the catalysts activity, since the catalyst with higher SSA, $Ni_2P$/CNT,

does not demonstrate the highest activity. On the other hand, Fe based catalysts demonstrate comparable BET SSA but different ECSA which is reflected on the catalyts activity.

Ultimately, it is unclear whether ECSA or BET is more accurate for estimating the catalytically active surface area, the true active sites of the system. Therefore, report both ECSA and BET is recommended so the range of possible surface areas and specific activities can be considered.[52]

# 5 Conclusion

In this thesis, new metal-air catalysts were designed, synthesised and characterized for the oxygen reduction and evolution reactions. Catalysts $Ni_2P$, $Ni_2P$/CNT, $Ni_2P$-Fe/CNT and $Ni_2P$-$Fe_2O_3$/CNT were synthesized and subsequently tested in RDE to obtain the catalytic activity regarding ORR and OER. LSV was performed in a rotating disk electrode at 400, 900, 1600 and 2500 rpm for each catalyst in the potential range 1.1 V to 0.2 V for ORR and 1.2 V to 1.65 V for OER. To understand the behaviour of the catalysts physical and chemical characterization were done, such as SEM, EDX, TGA, XRD and XPS.

$Ni_2P$ and $Ni_2P$/CNT were successfully synthesized according to the characterization results, while new conceptualized catalysts $Ni_2P$-Fe/CNT and $Ni_2P$-$Fe_2O_3$/CNT need more synthesis optimization. The conceptualized Fe/CNT did not show the calculated amount of metallic iron in the catalyst. To get the desired amount of Fe pre-synthesis precursor composition needs to be changed. $Ni_2P$-$Fe_2O_3$/CNT and $Ni_2P$-Fe/CNT seemed to have changed during the phosporization in the tubular furnace. In $Ni_2P$-$Fe_2O_3$/CNT few Ni particles in $Ni_2P$ lattice structure might have been substituted by Fe atoms and possibly forming $Ni_{2-x}Fe_xP$. $Ni_2P$-Fe/CNT was also shown to have Fe-P in its composition.

Regarding the ORR reaction the catalysts were compared with the benchmark for ORR, Pt/C, and the results demonstrated that the catalysts did not reach the high catalytic activity of Pt/C. Nonetheless, it was proved that adding CNT as a support provides better $E_{\text{onset}}$ for ORR. On the other hand, the results for the OER reaction were quite positive since $Ni_2P$-$Fe_2O_3$/CNT reached a performance higher than the benchmark catalyst, Ir Black. The $E_{\text{onset}}$ for this catalyst is 1.48 V, 0.04 V lower than the $E_{\text{onset}}$ for Ir Black. Additionally, the overpotential at 10 $mA/cm^2$ for this catalyst also showed a satisfying result. The value obtained was 236 mV once more lower than the one obtained for the benchmark catalyst.

# 6 Assessment of the work done

## 6.1 Objectives Achieved

In this work the objective of creating a new catalyst which performs as a bi-functional catalyst for metal-air batteries was not achieved. Nonetheless, it was discovered a new catalyst that performs better than the benchmark one for the OER. The electrochemical characterization of the catalysts was successfully developed as the measurements done for the catalysts presented reproducible results which ensured the reliability of the results obtained. Regarding the physical characterization methods, they seemed to prescribe a different catalyst than the one initially idealized since some of the measurements were not completely clear and are in need of further study.

## 6.2 Limitations and Future work

In order to improve and perfection the catalyst synthesis more time was needed in order to test different variables, for instance change the ratio of the materials or even test different synthesis methods. Even then, more time was needed to not only fully characterise the catalysts, but also to better understand its behaviour. For future work, it is crucial that further investigations keep on being done towards the increase of ORR and OER kinetics in order to improve metal-air batteries performance.

## 6.3 Final Assessment

The realization of this work allowed me to deepen my knowledge in electrochemistry and provided me insight in various topics that were completely new for me. This project gave me an insight on different techniques regarding electrochemical characterisation and physical analysis. Besides that, this whole experience made me go out of my comfort zone and made me grow not only in a professional level, as well as in a personal point of view. All of the hard work months that I have been through come out as rewarding and I really appreciate having the opportunity to embrace this experience.

# 7 References

[1] M. Fowler, Z. Chen, M. G. Park, Z. P. Cano, A. Yu, and J. Fu, "Electrically Rechargeable Zinc-Air Batteries: Progress, Challenges, and Perspectives," *Advanced Materials*, vol. 29, pp. 1–34, 2016.

[2] Z. L. Wang, D. Xu, J. J. Xu, and X. B. Zhang, "Oxygen electrocatalysts in metal-air batteries: From aqueous to nonaqueous electrolytes," 2014.

[3] M. A. Rahman, X. Wang, and C. Wen, "High Energy Density Metal-Air Batteries: A Review," *Journal of The Electrochemical Society*, vol. 160, no. 10, pp. A1759–A1771, 2013.

[4] J. S. Lee, S. T. Kim, R. Cao, N. S. Choi, M. Liu, K. T. Lee, and J. Cho, "Metal-air batteries with high energy density: Li-air versus Zn-air," 2011.

[5] D. Wittmaier, S. Aisenbrey, N. Wagner, and K. A. Friedrich, "Bifunctional, carbon-free nickel/cobalt-oxide cathodes for lithium-air batteries with an aqueous alkaline electrolyte," *Electrochimica Acta*, vol. 149, pp. 355–363, 2014.

[6] J. Zhang, Z. Zhao, Z. Xia, and L. Dai, "A metal-free bifunctional electrocatalyst for oxygen reduction and oxygen evolution reactions," *Nature Nanotechnology*, vol. 10, no. 5, pp. 444–452, 2015.

[7] C. Hu and L. Dai, "Carbon-Based Metal-Free Catalysts for Electrocatalysis beyond the ORR," *Angewandte Chemie - International Edition*, vol. 55, no. 39, pp. 11 736–11 758, 2016.

[8] "DLR at a glance." [Online]. Available: www.dlr.de, Date accessed 2019-02-21

[9] Gianfranco Pistoia, "Chapter 1 - Basic Battery Concepts," *Batteries for Portable Devices*, pp. 1–15, 2005.

[10] Y. Zong, F. W. T. Goh, D. Wuu, X. Ge, T. S. A. Hor, A. Sumboja, B. Li, T. An, and Z. Liu, "Oxygen Reduction in Alkaline Media: From Mechanisms to Recent Advances of Catalysts," *ACS Catalysis*, vol. 5, no. 8, pp. 4643–4667, 2015.

[11] R. Ahmed, "Durable High Surface Area Electrodes for Rechargeable Zinc Air Batteries," Tech. Rep., 2015.

[12] L. Khotseng, "Electrocatalysts for Fuel Cells and Hydrogen Evolution - Theory to Design, Oxygen Reduction Reaction," *Heavy Metal Removal with Phytoremediation*, vol. Chapter 2, 2016.

[13] L. Li, Z.-w. Chang, and X.-B. Zhang, "Recent Progress on the Development of Metal-Air Batteries," *Advanced Sustainable Systems*, vol. 1, no. 10, 2017.

[14] N. T. Suen, S. F. Hung, Q. Quan, N. Zhang, Y. J. Xu, and H. M. Chen, "Electrocatalysis for the oxygen evolution reaction: Recent development and future perspectives," *Chemical Society Reviews*, vol. 46, no. 2, pp. 337–365, 2017.

[15] H. Bandal, K. K. Reddy, A. Chaugule, and H. Kim, "Iron-based heterogeneous catalysts for oxygen evolution reaction; change in perspective from activity promoter to active catalyst," *Journal of Power Sources*, vol. 395, no. February, pp. 106–127, 2018. [Online]. Available: https://doi.org/10.1016/j.jpowsour.2018.05.047

[16] R. . Frydendal, I. . Chorkendorff, and Stephens, "Improving performance of catalysts for water electrolysis The MnOx case," Ph.D. dissertation, Department of Physics, Technical University of Denmark, 2015.

[17] R. O'Hayre, D. M. Barnett, and F. B. Prinz, "The Triple Phase Boundary," *Journal of The Electrochemical Society*, 2005.

[18] T. Danner, S. Eswara, V. P. Schulz, and A. Latz, "Characterization of gas diffusion electrodes for metal-air batteries," *Journal of Power Sources*, vol. 324, pp. 646–656, 2016.

[19] Y. Li and J. Lu, "Metal-Air Batteries: Will They Be the Future Electrochemical Energy Storage Device of Choice?" 2017.

[20] M. Shao, Q. Chang, J. P. Dodelet, and R. Chenitz, "Recent Advances in Electrocatalysts for Oxygen Reduction Reaction," *Chemical Reviews*, vol. 116, no. 6, pp. 3594–3657, 2016.

[21] R. Cao, J. S. Lee, M. Liu, and J. Cho, "Recent progress in non-precious catalysts for metal-air batteries," *Advanced Energy Materials*, vol. 2, no. 7, pp. 816–829, 2012.

[22] S. Liang and C. Liang, "High-density cobalt nanoparticles encapsulated with nitrogen-doped carbon nanoshells as a bifunctional catalyst for rechargeable zinc-air battery," *Materials*, vol. 12, no. 2, 2019.

[23] W. Wang, X. Wei, D. Choi, X. Lu, G. Yang, and C. Sun, "Electrochemical cells for medium- and large-scale energy storage: Fundamentals," *Advances in Batteries for Medium and Large-Scale Energy Storage: Types and Applications*, pp. 3–28, 2014.

[24] T. Lohmann, R. Liedtke, A. Kojic, J. Ahmed, J. Christensen, B. Kozinsky, R. S. Sanchez-Carrera, and P. Albertus, "A Critical Review of Li/Air Batteries," *Journal of The Electrochemical Society*, vol. 159, no. 2, pp. R1–R30, 2011.

[25] "Chapter 18 - Exergy Analysis of Fuel Cell Systems," *EXERGY*, pp. 363–382, 2013.

[26] A. Molina, J. González, E. Laborda, and R. G. Compton, "On the meaning of the diffusion layer thickness for slow electrode reactions," *Physical Chemistry Chemical Physics*, vol. 15, no. 7, pp. 2381–2388, 2013.

[27] Y.-h. Fang and Z.-p. Liu, "Tafel Kinetics of Electrocatalytic Reactions : From Experiment to First- Principles," 2014.

[28] T. Jaramillo, "Energy Tutorial : Electrocatalysis," Electrochemical Energy Conversion and Storage Stanford University, Tech. Rep., 2012.

[29] N. R. Elezović, B. M. Babić, L. J. Vračar, and N. V. Krstajić, "Oxygen reduction at platinum nanoparticles supported on carbon cryogel in alkaline solution," *Journal of the Serbian Chemical Society*, vol. 72, no. 7, pp. 699–708, 2007.

[30] S. S. Kocha, J. W. Zack, B. S. Pivovar, R. M. Richards, and K. Shinozaki, "Oxygen Reduction Reaction Measurements on Platinum Electrocatalysts Utilizing Rotating Disk Electrode Technique," *Journal of The Electrochemical Society*, vol. 162, no. 10, 2015.

[31] Y. C. M. P. P.-Y. A. C. Guangfu Li, Lawrence Anderson, "New insights into evaluating catalyst activity and stability of oxygen evolution reactions in alkaline media," *Sustainable Energy & Fuels*, 2017.

[32] C. Du, Q. Tan, G. Yin, and J. Zhang, *Chapter 5 - Rotating Disk Electrode Method*. Elsevier B.V., 2014.

[33] W. Oelßner, F. Berthold, and U. Guth, "The iR drop – well-known but often underestimated in electrochemical polarization measurements and corrosion testing," no. 6, pp. 455–466, 2006.

[34] T. Shinagawa, A. T. Garcia-Esparza, and K. Takanabe, "Insight on Tafel slopes from a microkinetic analysis of aqueous electrocatalysis for energy conversion," *Scientific Reports*, vol. 5, no. September, pp. 1–21, 2015.

[35] L. Feng, H. Vrubel, M. Bensimon, and X. Hu, "Easily-prepared dinickel phosphide (Ni2P) nanoparticles as an efficient and robust electrocatalyst for hydrogen evolution," *Physical Chemistry Chemical Physics*, vol. 16, no. 13, pp. 5917–5921, 4 2014.

[36] H. A. Asmaly, B. Abussaud, Ihsanullah, T. A. Saleh, V. K. Gupta, and M. A. Atieh, "Ferric oxide nanoparticles decorated carbon nanotubes and carbon nanofibers: From synthesis to enhanced removal of phenol," *Journal of Saudi Chemical Society*, vol. 19, no. 5, pp. 511–520, 9 2015.

[37] X. Zhang, X. Yu, L. Zhang, F. Zhou, Y. Liang, and R. Wang, "Molybdenum Phosphide/Carbon Nanotube Hybrids as pH-Universal Electrocatalysts for Hydrogen Evolution Reaction," *Advanced Functional Materials*, vol. 28, no. 16, 4 2018.

[38] Y. Chen, T. Tian, J. Tan, G. Li, M. Pan, and Q. Zhong, "Electrochemical study of temperature and Nafion effects on interface property for oxygen reduction reaction," *Ionics*, vol. 24, no. 12, pp. 3905–3914, 2018.

[39] Y. Garsany, I. L. Singer, and K. E. Swider-Lyons, "Impact of film drying procedures on RDE characterization of Pt/VC electrocatalysts," *Journal of Electroanalytical Chemistry*, vol. 662, no. 2, pp. 396–406, 2011.

[40] A. Dutta and N. Pradhan, "Developments of Metal Phosphides as Efficient OER Precatalysts," *Journal of Physical Chemistry Letters*, vol. 8, no. 1, pp. 144–152, 2017.

[41] H. Wang, W. Wang, Y. Y. Xu, M. Asif, H. Liu, and B. Y. Xia, "Ball-milling synthesis of Co 2 P nanoparticles encapsulated in nitrogen doped hollow carbon rods as efficient electrocatalysts," *Journal of Materials Chemistry A*, vol. 5, no. 33, pp. 17 563–17 569, 2017.

[42] T. Zhou, Y. Du, S. Yin, X. Tian, H. Yang, X. Wang, B. Liu, H. Zheng, S. Qiao, and R. Xu, "Nitrogen-doped cobalt phosphate@nanocarbon hybrids for efficient electrocatalytic oxygen reduction," *Energy and Environmental Science*, vol. 9, no. 8, pp. 2563–2570, 2016.

[43] J. Li, J. Li, X. Zhou, Z. Xia, W. Gao, Y. Ma, and Y. Qu, "Highly Efficient and Robust Nickel Phosphides as Bifunctional Electrocatalysts for Overall Water-Splitting," *ACS Applied Materials and Interfaces*, vol. 8, no. 17, pp. 10 826–10 834, 2016.

[44] Y. Wang, B. Kong, D. Zhao, H. Wang, and C. Selomulya, "Strategies for developing transition metal phosphides as heterogeneous electrocatalysts for water splitting," *Nano Today*, vol. 15, pp. 26–55, 2017.

[45] G. Zhang, J. Yuan, Y. Liu, W. Lu, N. Fu, W. Li, and H. Huang, "Boosting the oxygen evolution reaction in non-precious catalysts by structural and electronic engineering," *Journal of Materials Chemistry A*, vol. 6, no. 22, pp. 10 253–10 263, 2018.

[46] Y. Wang, J. Li, and Z. Wei, "Transition-metal-oxide-based catalysts for the oxygen reduction reaction," *Journal of Materials Chemistry A*, vol. 6, no. 18, pp. 8194–8209, 2018.

[47] Feihong Song, "Development and characterization of nanostructured oxygen electrocatalysts for anode of PEM electrolyzer," 2016.

[48] K. Liu, F. Wang, P. He, T. A. Shifa, Z. Wang, Z. Cheng, X. Zhan, and J. He, "The Role of Active Oxide Species for Electrochemical Water Oxidation on the Surface of 3d-Metal Phosphides," *Advanced Energy Materials*, vol. 8, no. 15, pp. 1–7, 2018.

[49] W. L. Kwong, C. C. Lee, and J. Messinger, "Scalable two-step synthesis of nickel-iron phosphide electrodes for stable and efficient electrocatalytic hydrogen evolution," *Journal of Physical Chemistry C*, vol. 121, no. 1, pp. 284–292, 2017.

[50] K. Tang, X. Wang, M. Wang, Y. Xie, J. Zhou, and C. Yan, "Ni/Fe Ratio Dependence of Catalytic Activity in Monodisperse Ternary Nickel Iron Phosphide for Efficient Water Oxidation," *ChemElectroChem*, vol. 4, no. 9, pp. 2150–2157, 2017.

[51] M. Wang, C. Zhang, T. Meng, Z. Pu, H. Jin, D. He, J. Zhang, and S. Mu, "Iron oxide and phosphide encapsulated within N,P-doped microporous carbon nanofibers as advanced tri-functional electrocatalyst toward oxygen reduction/evolution and hydrogen evolution reactions and zinc-air batteries," *Journal of Power Sources*, vol. 413, no. December 2018, pp. 367–375, 2019.

[52] S. Jung, C. C. L. McCrory, I. M. Ferrer, J. C. Peters, and T. F. Jaramillo, "Benchmarking nanoparticulate metal oxide electrocatalysts for the alkaline water oxidation reaction," *Journal of Materials Chemistry A*, vol. 4, no. 8, pp. 3068–3076, 2016.

# A Appendix

## A.1 Other Results

Figure 36, presents the results obtained for Pt regarding the ORR activity and the calculated number of electrons transferred.

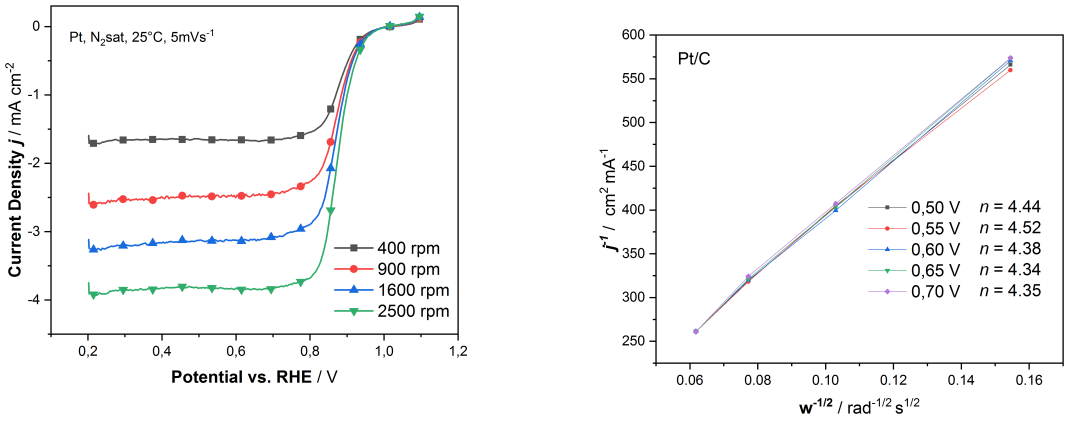



Figure 36: ORR and K-L plots for Pt/C

EDX results for $Fe_2O_3$/CNT are presented in figure 37 and table 11.

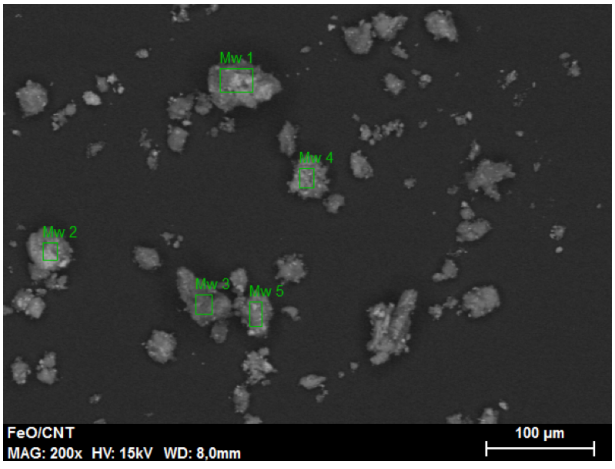



Figure 37: $Fe_2O_3$/CNT EDX

Table 11: Mass % spectrum of $Fe_2O_3$/CNT

| Spectrum wt% | C | O | Mg | S | Fe |
|---|---|---|---|---|---|
| Mw 1 | 37.96 | 20.99 | - | 0.48 | 30.57 |
| Mw 2 | 25.32 | 29.26 | - | 0.50 | 44.92 |
| Mw 3 | 64.19 | 19.13 | - | 0.58 | 16.10 |
| Mw 4 | 38.07 | 18.28 | - | 0.78 | 42.88 |
| Mw 5 | 44.28 | 27.22 | 0.07 | 0.54 | 27.88 |

EDX results for Fe/CNT are presented in figure 38 and table 12.

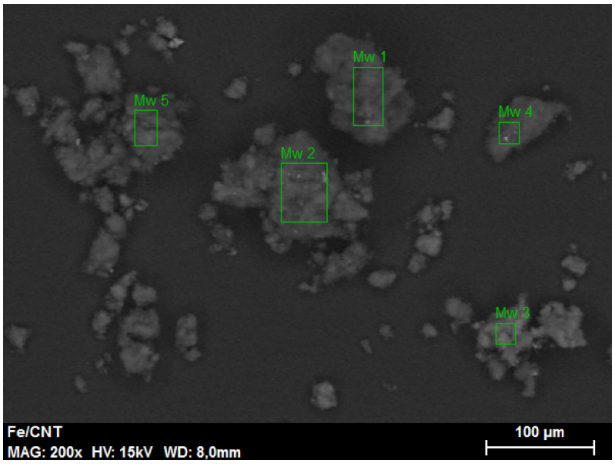



Figure 38: Fe-CNT EDX

Table 12: Mass % spectrum of Fe-CNT

| Spectrum wt% | C | O | S | Fe |
|---|---|---|---|---|
| Mw 1 | 73.69 | 12.70 | 0.53 | 13.09 |
| Mw 2 | 77.40 | 10.88 | 0.51 | 11.21 |
| Mw 3 | 64.04 | 16.29 | 0.33 | 19.34 |
| Mw 4 | 79.51 | 12.46 | 0.28 | 7.75 |
| Mw 5 | 77.24 | 13.71 | 0.34 | 8.72 |

For the calculation of $c_{dl}$ values, it was considered the middle current value measured for 1 V, divided by 2 and by the surface area of the GCE [*i/2* in mA/cm$^2$]. It was then plotted *i/2* vs. the scan rates in mV/s. The slope of the linear regression of the values indicates the $c_{dl}$ in $\mu$F/cm$^2$

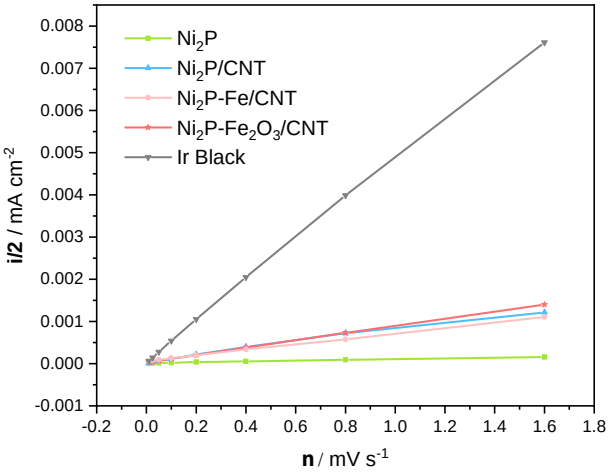



Figure 39: $c_{\mathrm{dl}}$ calculations.

Regarding the TGA measurement in figure 40 it is presented the burning of a pure sample of CNT.

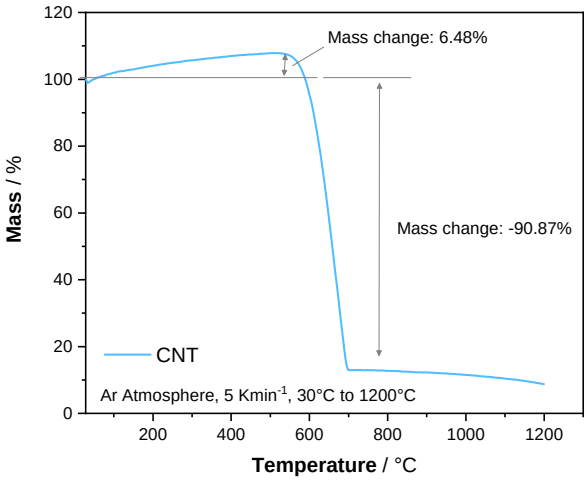
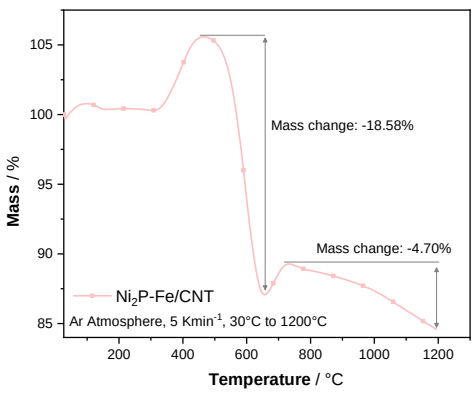
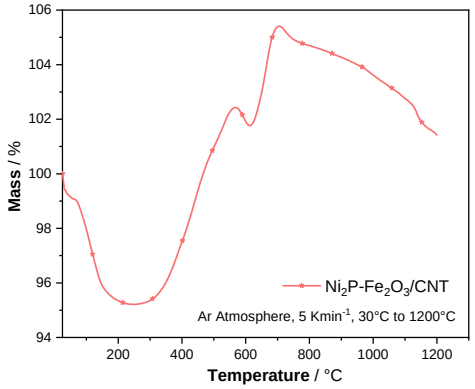



Figure 40: CNT TGA

In the following figures, 41a and 41b, are presented the results obtained for $Ni_2P$-Fe/CNT and for $Ni_2P$-$Fe_2O_3$/CNT, respectively.




(a) $Ni_2P$-Fe/CNT TGA




(b) $Ni_2P$-$Fe_2O_3$/CNT TGA

## A.2 Equipment used

In picture 42 is the Tubular furnace used for the synthesis of the catalysts.

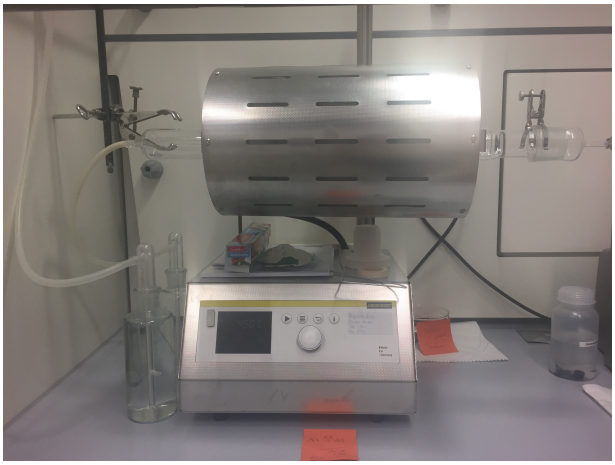


Figure 42: Tubular furnace

The RDE used for electrochemical measurements in this thesis is presented in the picture below, figure 43.

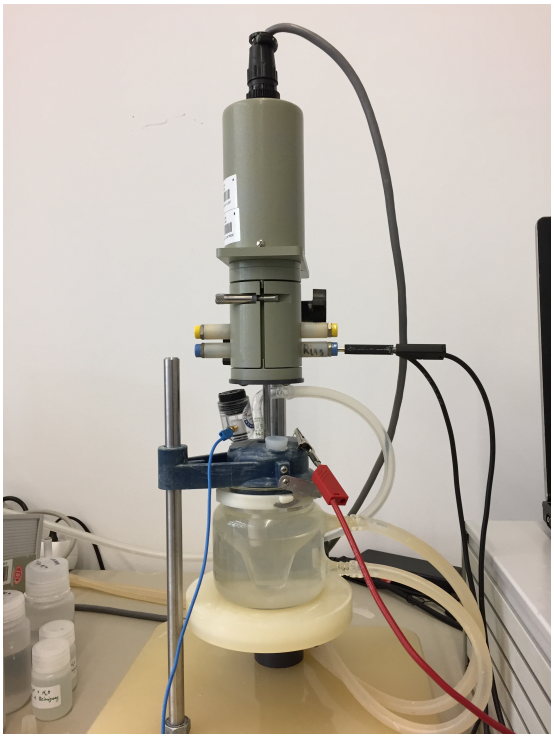


Figure 43: RDE